Large-scale flow toward low-velocity anomalies reconciles seismic and geodynamic constraints in the deepest mantle beneath Alaska

Jonathan Wolf[1,2,3]

[1]Department of Earth and Planetary Sciences, University of California, Santa Cruz, CA 95064, USA
[2]Department of Earth and Planetary Science, University of California, Berkeley, CA 94720, USA
[3]Miller Institute for Basic Research in Science, Berkeley, CA 94720, USA

Key Points:

- Coherent large-scale lowermost mantle anisotropy is observed beneath Alaska and interpreted using mineral physics constraints.
- The direction of shear is oriented approximately North-South (or South-North).
- Results support the first-order framework of flow directed away from mantle downwellings and toward low-velocity anomalies.

Corresponding author: Jonathan Wolf, `wolf@ucsc.edu`

Abstract

Deep mantle downwellings are typically located away from the two Large Low-Velocity Provinces (LLVPs) in Earth's mantle. Geodynamic models based on global seismic tomography generally predict that convective flow at the core-mantle boundary (CMB) spreads laterally away from downwelling regions and towards LLVPs. While this offers a framework for understanding large-scale deformation in the lowermost mantle, it has yet to be confirmed by seismic constraints. This study investigates seismic anisotropy and wave reflections in the deepest mantle beneath Alaska, linking a known reflector to the inferred deformation. To capture large-scale deformation, the analysis utilizes waves with long raypaths through the deepest mantle. Mantle shear direction is then determined using global wavefield simulations that incorporate mineral physics constraints. The inferred North-South shear direction agrees with findings for an adjacent region beneath the northeastern Pacific Ocean, together forming a continuous $\sim 3000\,\mathrm{km}\times 3000\,\mathrm{km}$ region where the inferred southward shear aligns with geodynamic model predictions. These results support a first-order framework of lowermost mantle deformation driven by flow away from downwellings and toward LLVPs.

Plain Language Summary

Two large regions of below-average seismic velocities exist in Earth's mantle, surrounded by higher velocities. Computational simulations predict that Earth's mantle material slowly flows away from colder high-velocity regions towards hotter regions with low velocities. These considerations offer a framework to understand deformation in Earth's deepest mantle. Deformation due to convective flow causes seismic waves to have speeds that depend on their direction of travel and vibration, a phenomenon called seismic anisotropy. In this study, I use waves from distant earthquakes to investigate deformation in the lowermost mantle beneath Alaska. The results indicate North-South directed deformation across a $\sim 3000\,\mathrm{km}\times 3000\,\mathrm{km}$ region beneath Alaska and the northeastern Pacific Ocean. This supports the idea that large-scale deformation is controlled by flow towards these low-velocity anomalies, even in regions far from them.

1 Introduction

Although large-scale deformation in the asthenosphere, the top of Earth's convecting interior, is well understood to be dominated by present-day plate motions (e.g., Hager & O'Connell, 1979; Tanimoto & Anderson, 1984), no comparable paradigm exists for the lowermost mantle, which forms the lower boundary of convective flow. Geodynamic models that infer density anomalies from seismic velocity structure commonly predict converging flow toward the mantle's antipodal large low-velocity provinces (LLVPs) (e.g., McNamara et al., 2002; McNamara et al., 2003; Walker et al., 2011; Forte et al., 2015; Li et al., 2024), whereas plate-reconstruction-based models often yield more complex large-scale flow patterns (e.g., Flament, 2018; Ward et al., 2024; Roy et al., 2025a). In the upper mantle, large-scale shear in the asthenosphere was first predicted from geodynamic models to align with plate motions (Hager & O'Connell, 1979); this prediction was later confirmed by observations of seismic anisotropy (e.g., Tanimoto & Anderson, 1984; Anderson, 1995), which refers to the dependence of seismic wave speeds dependent on propagation and/or polarization direction. However, obtaining robust flow inferences from seismic anisotropy in the lowermost mantle is far more challenging. Reasons include the unavailability of surface-wave constraints, the influence of anisotropy at multiple depths on body-wave measurements, and the difficulty of performing mineral physics experiments under the extreme temperatures and pressures of the deepest mantle (Nowacki et al., 2011; Romanowicz & Wenk, 2017; Wolf, Li, Long, & Garnero, 2024).

The primary reason why flow in the deepest mantle has only been inferred from seismic anisotropy in a few regions is insufficient ray sampling in most areas. Challenges include the limited number of regional flow constraints, and that locally inferred flow does not necessarily match large-scale flow patterns, analogous to how asthenospheric flow can deviate from plate motions, such as in subduction zones (e.g., Long, 2013). Furthermore, most prior flow inferences rely on ray-theoretical assumptions (e.g., Ford et al., 2015; Creasy et al., 2019; Pisconti et al., 2023), which have been often shown to be inaccurate (e.g., Komatitsch et al., 2010; Parisi et al., 2018; Nowacki & Wookey, 2016; Wolf et al., 2022).

The lowermost mantle beneath Alaska is exceptionally well sampled by shear waves that diffract along (S_{diff}, Figure 1a) and reflect off (ScS, Figure 1a) the core–mantle boundary (CMB). These phases are sensitive to a broad volume in the lowermost mantle, enabling the detection of regional-scale flow patterns suitable for comparison with global geodynamic predictions from long-wavelength tomography. While no previous study has determined the mantle flow direction beneath Alaska, constraints immediately to the south, beneath the northeastern Pacific Ocean (Wolf & Long, 2022), suggest either southward or northward shear, consistent with geodynamic predictions of predominantly southward flow (e.g., Forte et al., 2015; Li et al., 2024) (Figure 1b). Together, Alaska and the northeastern Pacific represent a large portion of the lowermost mantle where large-scale flow patterns can be evaluated over a continuous area, providing an opportunity to assess whether the observed agreement with geodynamic models is coincidental or reflects systematic large-scale flow.

The structure and dynamic processes of the lowermost mantle beneath Alaska can be constrained not only from seismic anisotropy but also from a well-documented seismic reflector located a few hundred kilometers above the CMB, which defines the upper boundary of the D$''$ layer (e.g., Lay & Helmberger, 1983; Cobden et al., 2015). This reflector has not yet been explicitly considered in interpretations of seismic anisotropy beneath the northeastern Pacific Ocean (e.g., Long, 2009; Nowacki et al., 2010; Asplet et al., 2020, 2023; Suzuki et al., 2021; Wolf & Long, 2022, 2023), but could provide complementary evidence reinforcing previous inferences of slab-related deformation.

In this study, I investigate the dynamics of the lowermost mantle beneath Alaska. I use global wavefield simulations to simultaneously constrain properties of the D$''$ reflector and interpret shear-wave splitting measurements in terms of mantle shear, incorporating a broad range of mineral physics constraints. The resulting models reveal a mantle shear direction that is consistent across a large region, including both the lowermost mantle beneath Alaska and the northeastern Pacific, and aligns well with the North–South flow predicted by geodynamic models. This suggests large-scale lowermost mantle flow directed away from downwelling zones towards LLVPs.

2 D$''$ reflector beneath Alaska

The existence of a D$''$ reflector beneath Alaska and parts of the northeastern Pacific Ocean is well-established (e.g., Lay & Helmberger, 1983; Lay & Young, 1991; Chambers & Woodhouse, 2006; Cobden et al., 2015). Here, I investigate its properties using reflections that arrive between the S and ScS phases, called SdS (Figure 1a).

This study analyzes seven events with depths greater than 200 km that occurred near the Sea of Okhotsk and were recorded at stations across the United States. Seismograms are displayed as S-aligned stacks in 0.2° distance increments (Figure 2a,b; Supplementary Figure S1). To assess the presence or absence of the D″ reflector, record sections are constructed for 5° backazimuthal ranges. Where a reflector is identified, data for each event are subsequently stacked into a record section spanning a larger backazimuthal range, thereby enhancing the visibility of the reflection by reducing noise (Figure 2a,b; Supplementary Figure S1).

The D″ reflector extends across much of the lowermost mantle beneath Alaska and the northeastern Pacific Ocean (Figure 2c). Where the reflector is not observed, it may still be present; apparent absences largely coincide with regions of poor sampling, where fewer seismograms contribute to the stacks and the signal-to-noise ratio is consequently lower. Overall, the D″ reflector is identified in 73% of the records; the distribution of these reflection points is displayed in Figure 2c. Ray-theoretical travel time predictions suggest that the D″ reflector is inclined, descending from roughly 200 km above the CMB in the western part of the study region to about 120 km in the east (Figure 2a,b).

I conduct global seismic wavefield simulations using AxiSEM3D (Leng et al., 2016, 2019; Fernando et al., 2024), which account for Earth's ellipticity and attenuation as defined by the preliminary reference Earth model (PREM, Dziewonski & Anderson, 1981) to obtain a first-order estimate of the velocity change across the D″ discontinuity. Earthquake source parameters are obtained from the Global CMT Catalog (Ekström et al., 2012), and synthetic seismograms are calculated down to periods of 2 s. The isotropic version of PREM serves as the baseline velocity model for these simulations, to which a discontinuity is added in the lowermost mantle. For these simulations, I derive a first-order estimate of the velocity contrast by visually comparing reflector amplitudes of synthetics and real-data record sections. While a more detailed estimate could be obtained using systematic waveform fitting, this would require overcoming the challenge of noise which often obscures these weak phases; but an exact estimate of the velocity contrast is not critical for the purpose of this work. These simulations suggest an approximate velocity contrast of ∼2 % in the west, increasing to ∼4 %–8 % in the east (Supplementary Figures S2, S3).

3 Shear-wave splitting measurements

In the presence of seismic anisotropy, a shear wave splits into two components: one propagating faster and the other slower. The resulting delay time, δt, between these components and the polarization direction of the fast component relative to the backazimuth, ϕ' (Figure 3), can be determined. In this reference frame, $\phi' = 0°$ corresponds to a vertical fast polarization direction in D$''$ (Nowacki et al., 2010). In contrast to ϕ', upper mantle studies usually use ϕ which is measured relative to geographic North. A third measurable quantity is the splitting intensity, SI (Chevrot, 2000), which can be expressed as

$$SI = -2\frac{C_{90}(t)C'0(t)}{|C'0(t)|^2} \approx \delta t \sin(-2\phi') \ , \tag{1}$$

where $C_{90}(t)$ denotes the horizontal seismogram component oriented 90° from the initial polarization of the incoming wave, and C'_0 is the time derivative of the component aligned with the initial polarization. For core-refracted waves undergoing a P–SV conversion at the CMB, C_0 corresponds to the radial component. For S$_{\text{diff}}$ waves, provided strict precautions are taken (Wolf et al., 2023; Wolf, Long, & Frost, 2024), C_0 corresponds to the transverse component. For ScS waves, C_0 can generally show in an arbitrary direction, dependent of the source mechanism, but is readily identified as the long axis of the ScS particle motion (Wookey et al., 2005; Nowacki et al., 2010; Wolf et al., 2022).

Splitting measurements are performed using a modified version of SplitRacerAuto (Reiss & Rümpker, 2017; Link et al., 2022), as described in detail by Wolf, Becker, et al. (2025), who also made this version publicly available. In principle, the measured shear-wave splitting reflects anisotropy accumulated anywhere along the raypath. However, under the common assumption that the bulk of the lower mantle is nearly isotropic (Niu & Perez, 2004; Wang & Wen, 2004; Meade et al., 2005), the interpretation can be simplified: S$_{\text{diff}}$ and ScS phases are sensitive primarily to anisotropy in the source-side upper mantle, the receiver-side upper mantle, and the lowermost mantle. For both S$_{\text{diff}}$ and ScS, explicit ray-theoretical anisotropy corrections are avoided, which have been shown to be unreliable in many cases (e.g., Wolf & Long, 2024). Splitting measurements are performed on data bandpass-filtered to retain periods between 6 and 25 s. All splitting measurements used in this study are appended as supplementary text files.

3.1 Sdiff measurements

I follow the strategy of Wolf et al. (2023) to measure $\mathrm{S_{diff}}$ splitting, aiming primarily to isolate the effects of lowermost mantle anisotropy on $\mathrm{S_{diff}}$ waves while avoiding the misinterpretation of isotropic influences on the $\mathrm{S_{diff}}$ wavefield (e.g., Komatitsch et al., 2010; Parisi et al., 2018) as signatures of anisotropy. Key aspects of this approach involve selecting only seismic events whose focal mechanisms would produce transversely polarized $\mathrm{S_{diff}}$ waves in the absence of anisotropy, and interpreting only those $\mathrm{S_{diff}}$ measurements for which the corresponding SKS phase (Figure 1a) from the same source–receiver pair shows null splitting (Figure 4a). Further details are given in Wolf et al. (2023).

All measurements, plotted by their ϕ' values (displayed as the angle relative to north), are shown in Figure 4b. The study region is sampled by two distinct directional swaths, which yield similar delay times but ϕ' values that are approximately orthogonal.

3.2 ScS measurements

To determine ScS splitting measurements, I follow the approach of Wolf and Long (2024). I do not apply explicit corrections for source- or receiver-side upper mantle anisotropy. Instead, I restrict the analysis to ScS phases whose corresponding S waves are unsplit (Figure 5a), and assume that for these S-ScS pairs, ScS is likewise not affected by upper mantle anisotropy. I further limit the dataset to epicentral distances between 60° and 70°, a range in which the behavior of the ScS radial component upon reflection at the CMB is well understood. Because ScS splitting depends on the wave's initial polarization and reflects seismic anisotropy before and after reflection off the CMB (which is essentially a two-layer case), measurements for the same lowermost mantle location, when sampled from the same azimuth, will generally yield different results. For further details, I refer to Wolf and Long (2024).

Compiling all measurements reveals two distinct ScS fast polarization directions, depending on the wave's source polarization (Figure 5b). For similar source polarizations and lowermost mantle sampling directions, results are consistent, supporting their robustness.

4 Inference of shear direction

The CMB is a horizontal boundary layer of mantle convection; therefore, flow in the lowermost mantle is likely predominantly horizontal. The lowermost mantle beneath and near Alaska is thought to host ancient subducted slab remnants (e.g., Asplet et al., 2020; Suzuki et al., 2021; Wolf, Li, & Long, 2024; Wolf, Romanowicz, et al., 2025), which likely contribute to the dominantly horizontal deformation. To model shear-wave splitting measurements, I therefore assume horizontal simple shear deformation.

For my analysis, no prior assumptions about the mineralogy are made. Instead, I model the anisotropy of bridgmanite (Br), post-perovskite (pPv), and ferropericlase (Fp), using a variety of previously suggested slip systems. The slip system is important, as it governs the development of crystallographic preferred orientation during deformation, thereby establishing the link between the macroscopic flow field and the resulting seismic anisotropy. However, since experimental constraints at deep-mantle conditions remain challenging and yield conflicting results regarding the dominant active mechanisms (e.g., Romanowicz & Wenk, 2017), it is essential to evaluate a broad ensemble of potential slip systems rather than relying on a single model. The elastic tensors for these minerals are taken from the library of Creasy et al. (2020). Because the region beneath Alaska is characterized by high seismic velocities, suggesting cooler than average temperatures, I exclusively use elastic tensors based on mineral physics experiments at temperatures of 3000 K or lower. These cooler conditions likely result in a relatively shallow depth for the Br-pPv phase transition (Murakami et al., 2004), and the observed D′′ discontinuity has been suggested to mark this transition (Cobden et al., 2015). This makes the dominant presence of pPv likely, but Br and Fp is not excluded in the modeling. I conduct fully three-dimensional global seismic wavefield simulations using AxiSEM3D down to 5 seconds, similar to those decribed above for the D′′ reflector analysis. Anisotropic regions are introduced into the lowermost mantle by embedding elastic tensors that represent the anisotropy in that layer. The anisotropic layer thickness is adjusted to lead to a realistic splitting strength for S_{diff} (similar to the splitting of the real data).

The source–receiver geometry used in the synthetic simulations is shown in Figure 6a. Given the strong consistency of S_{diff} splitting measurements across events with similar sampling paths, it is sufficient to model a single representative source–receiver pair (Figure 6a) and extract shear-wave splitting from the resulting synthetic seismograms. To explore directional dependence, each elastic tensor is rotated around the vertical axis (=the shear plane normal) in the horizontal simple-shear configuration (Figure 6b). These simulations are then mapped to backazimuth-dependent S_{diff} splitting patterns (Figure 7; Supplementary Figures S4-S5) for each elastic tensor.

Simulations of ScS splitting are more complex, as they must, in principle, be performed separately for each event owing to differences in source polarization. Here, two events with distinct source polarizations are selected, each representative of one of the two measured ScS fast polarization directions. Due to their shorter raypaths through D'', ScS phases are generally more sensitive to smaller-scale variations in seismic anisotropy than S_{diff}, a factor that may be reflected in the results, nonetheless S_{diff} and ScS simulations should lead to generally consistent results. Again, simulations are conducted for different rotations of the elastic tensors with respect to the shear plane normal (Supplementary Figures S6-S7).

As the primary goal is to constrain large-scale deformation, I first evaluate which elastic tensors and orientations can reproduce the observed S_{diff} splitting (Figure 7). My analysis reveals that five of the tested tensors fail to match the backazimuthal splitting pattern irrespective of the rotation angle applied (Supplementary Figure S4). Consequently, these scenarios can be excluded, unless the discrepancy arises from the limitation of the horizontal simple shear assumption. The remaining five, one Br and four pPv tensors, successfully replicate the observations. Notably, across all five viable deformation scenarios, the optimal fit converges on a consistent geometry, with the shear direction oriented at an angle of approximately $(-5\pm20)^\circ$ relative to North (Figure 7; Supplementary Figure S5).

Next, I assess whether these five candidate tensors also explain the ScS splitting measurements, for the same orientation inferred from the S_{diff} results. For one ScS event (20091210) real-data measurements and synthetics match, while for the other (20200915), ϕ' is nearly, but not fully, reproduced, and the predicted splitting strength is underestimated when using the same layer thicknesses as for S_{diff} (Figure 7). Overall, while broadly consistent with the S_{diff} inferences, the ScS results point to smaller-scale lateral variations in seismic anisotropy not captured by the S_{diff} splitting analysis.

5 Discussion

5.1 Interpreting results in the context of prior seismological studies

The presence of a prominent D$''$ reflector beneath Alaska and the northeastern Pacific Ocean is well-established (e.g., Lay & Helmberger, 1983; Lay & Young, 1996; Chambers & Woodhouse, 2006; Cobden et al., 2015). Its lateral extent has been estimated to exceed 1500 km (Lay & Young, 1996), though it has also been suggested to be intermittent (Chambers & Woodhouse, 2006). My stacking approach cannot resolve small-scale lateral variations, given the Fresnel zones, which represent the effective footprint of the reflected wavefield on the interface, with a size of several hundreds of kilometers for the analyzed D$''$ reflections. However, the reflector emerges as a coherent, large-scale feature, consistent with the interpretation of Lay and Young (1996).

Reported reflector depths range from 250 km to 300 km above the CMB (Lay & Young, 1996; Chambers & Woodhouse, 2006), which agrees with my estimates beneath western Alaska. The eastward increase in velocity contrast that I find was also noted by Lay and Young (1996). However, whereas prior studies have described the reflector as having either a relatively constant (e.g., Lay & Young, 1996) or undulating (e.g., Chambers & Woodhouse, 2006) depth, my findings indicate an eastward dip.

The presence of lowermost mantle anisotropy beneath Alaska has been reported by several previous studies (e.g., Lay & Young, 1991; Matzel et al., 1996; Garnero & Lay, 1997; Wysession et al., 1999; Suzuki et al., 2021). However, these earlier results did not determine the mantle shear direction. By contrast, in the northeastern Pacific Ocean, just south of Alaska and one of the most extensively studied regions for seismic anisotropy (e.g., Long, 2009; Nowacki et al., 2010; Suzuki et al., 2021; Asplet et al., 2020, 2023; Wolf, Frost, et al., 2024; Wolf et al., 2023), probable shear directions have been identified. In particular, measurements from $\mathrm{S_{diff}}$ waves (Wolf & Long, 2022), which are sensitive to large-scale ($\sim$ 1000 km) flow patterns, indicate a shear direction that is either North-South or, equivalently, south-north. All previous anisotropy studies for this region have invoked slab-driven processes to explain their anisotropy observations.

The presence of ancient slab remnants has also been suggested beneath Alaska and the northeastern Pacific Ocean, which have been named the Beaufort (van der Meer et al., 2018), Inzanagi and Telkhina Slabs (Suzuki et al., 2021). Their presence explains a visible D″ reflector, potentially due to reflections off their top or, alternatively, off the Br-pPv phase boundary, which is shallow due to their low temperatures. A recent global tomography model (Lei et al., 2020) shows a dipping, continuous high-shear-velocity region with increasing velocities to the East (Figure 8), which is consistent with a regional tomography study (Suzuki et al., 2021). This is generally in agreement with the properties I found for the D″ reflector. However, as a smoothed global tomography model, it inherently underestimates both the velocity contrast and the sharpness of the D″ boundary, which are quantified in this study.

While high seismic velocities alone do not necessarily confirm the presence of remnant slab material, the combined constraints from this and previous studies support a consistent interpretation of ancient slab remnants in at least parts of the lowermost mantle beneath Alaska and the northeastern Pacific. The dynamics of these slabs induce shear deformation of the mantle, influencing both isotropic seismic velocities and anisotropy.

5.2 Reconciling seismological and geodynamic constraints for the Alaska-northeastern Pacific region

Geodynamic models of mantle flow based on global seismic tomography do not fully capture small-scale changes in mantle flow, such as upwelling near deep mantle plumes, which previous seismic anisotropy studies have suggested (e.g., Ford et al., 2016; Wolf, Li, Long, & Garnero, 2024). While recent geodynamic models have demonstrated the capability to capture smaller-scale flow patterns and link them to seismic anisotropy (Hu et al., 2025; Hu & Gurnis, 2025; Roy et al., 2025a, 2025b), the structures associated with them are often poorly resolved in global tomography. Even when they are resolved, tomography-based geodynamic models face challenges in accurately reproducing their dynamics (e.g., Li et al., 2024). The lowermost mantle phase with the broadest sensitivity, most similar to the resolution capabilities of such tomography-based geodynamic models, is S_{diff}.

I demonstrate in this study that the region of large-scale North-South shear deformation, previously identified beneath the northeastern Pacific Ocean, extends approximately 1500 km northwards beneath Alaska. This creates a vast region, approximately 3000 km × 3000 km, with a consistent large-scale deformation pattern (Figure 8). It is important to note that this does not preclude the existence of smaller-scale deformation within this region, which could be investigated using seismic phases other than S_{diff}. For example, my ScS measurements, while generally consistent with the S_{diff} constraints, indicate the presence of some smaller-scale variability.

The large-scale deformation beneath Alaska and the northeastern Pacific Ocean is consistent with the dominant North-South flow toward the Pacific LLVP predicted by geodynamic flow models based on global seismic tomography (e.g., Forte et al., 2015; Li et al., 2024). Although this does not constitute a full quantitative global comparison between anisotropy-inferred flow and geodynamic predictions, a challenging task given limited crossing-ray coverage in many regions, this study reveals an exceptionally large area exhibiting consistent mantle deformation. My results, however, appear inconsistent with a transition in deformation regime across my study region, from dominantly horizontal flow in the west to vertical flow in the east, as suggested in a recent geodynamic study (Roy et al., 2025a).

Beneath the northeastern Pacific Ocean and Alaska, geodynamically predicted flow directed away from downwellings and toward the LLVPs, even in distant regions, offers a plausible explanation for the observed large-scale deformation. If confirmed in other regions, this pattern could provide a general conceptual framework for understanding large-scale deformation in the lowermost mantle.

6 Conclusion

In this study, I investigate large-scale isotropic and anisotropic velocity variations in the lowermost mantle beneath Alaska to resolve the region's deformation geometry. My results confirm the presence of a high-velocity D'' reflector characterized by an eastward dip and increasing velocity contrast, both consistent with seismic tomography. Global wavefield modeling of seismic anisotropy, combined with mineral physics data, suggests a dominant North-South shear direction, extending a previously identified region of similar shear beneath the northeastern Pacific Ocean. The deformation within this approximately $3000\,\mathrm{km}\times3000\,\mathrm{km}$ area agrees with the simple conceptual idea that, to first order, convective flow spreads laterally away from downwelling regions and towards LLVPs, which has been quantified using geodynamic modeling calculations. This concept has the potential to become a suitable basis for a first-order understanding of large-scale lowermost mantle deformation.

7 Open Research

The Generic Mapping Tools (Wessel & Smith, 1998) and ObsPy (Beyreuther et al., 2010) were utilized in this study. Synthetic seismograms were computed using AxiSEM3D (Leng et al., 2016, 2019, 2020; Fernando et al., 2024). SplitRacerAUTO (Link et al., 2022), which was used to conduct all splitting measurements, is available at `https://www.geophysik.uni-frankfurt.de/64002762/Software`. The precise code version that I used to measure splitting is also available at `https://doi.org/10.5281/zenodo.14834413`.

All data used in this study are publicly available, and were downloaded from the following datacenters: CNDC (`https://www.earthquakescanada.nrcan.gc.ca/stndon/CNDC/index-en.php`), Earthscope (`http://service.iris.edu/`), NCEDC (`https://ncedc.org/`) (UC Berkeley Seismological Laboratory, 2014), RESIF (`https://seismology.resif.fr/`) (RESIF, 1995), SCEDC (`https://scedc.caltech.edu/`)(Caltech, 2014), and SSN (`http://www.ssn.unam.mx/`) (Instituto de Geofísica, Universidad Nacional Autónoma de México, México, 2024). The network codes and corresponding citations (if available) are as follows: AR, AZ (UC San Diego, (1982)), BK (Northern California Earthquake Data Center, (2014)), CC (Cascades Volcano Observatory/USGS, (2001)), CI (California Institute of Technology and United States Geological Survey Pasadena, (1926)), CN (Natural Resources Canada (NRCAN Canada), (1975)), CU (Albuquerque Seismological Laboratory (ASL)/USGS, (2006)), EP, GS (Albuquerque Seismological Laboratory (ASL)/USGS, (1980)), HW, II (Scripps Institution of Oceanography, (1986)), IM, IU (Albuquerque Seismological Laboratory/USGS, (2014)), IW (Albuquerque Seismological Laboratory (ASL)/USGS, (2003)), LB, LD (Lamont Doherty Earth Observatory (LDEO), Columbia University, (1970)), NE (Albuquerque Seismological Laboratory (ASL)/USGS, (1994)), NM, PE (Penn State University, (2004)), SC, TA (IRIS Transportable Array, (2003)), UO (University of Oregon, (1990)), US (Albuquerque Seismological Laboratory (ASL)/USGS, (1990)), UW (University of Washington, (1963)), XF (Grand and Ni, (2006)), XO (Gary Pavlis and Hersh Gilbert, (2011)), Y5, YX (Klemperer and Miller, (2010)), Z9 (Fischer, Hawman, and Wagner, (2010)).

Conflicts of interest

The author declares no competing interests.

Acknowledgments

Funding was received by the Miller Institute for Basic Research in Science at UC Berkeley. I am grateful for detailed comments by David Schlaphorst and an anonymous reviewer, which have helped me improve the manuscript.

Figures and Animations

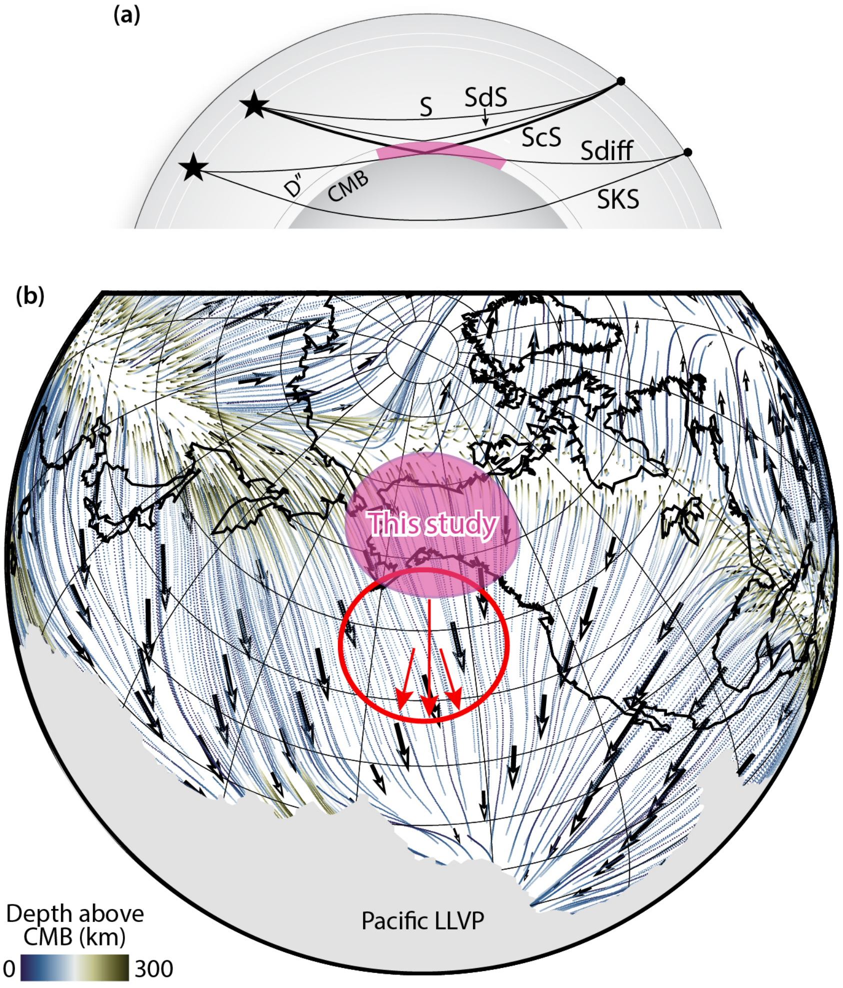

Figure 1. Setup and motivation of this study. (a) Schematic cross-section of Earth illustrating the seismic phases used in this study: direct S, core-reflected ScS, D''-reflected SdS, S_{diff} waves diffracting along the core-mantle boundary (CMB), and core-refracted SKS waves. The region of investigated seismic anisotropy is highlighted in pink. (b) Context of previous geodynamic (Li et al., 2024) and seismological (Wolf & Long, 2022) results. Colored lines depict trajectories of mantle tracers from the top of the D'' layer to 97.5 km above the CMB, derived from a geodynamic simulation (Case 1 of Li et al. (2024)). Line colors indicate the height of tracers above the CMB (see legend). Black arrows indicate the flow direction from this geodynamic simulation. The red ellipse marks the study region of Wolf and Long (2022), who suggested approximately southward flow consistent with the subsequent geodynamic results. The pink shaded area indicates the primary study region in this work. Gray shading denotes the Pacific LLVP, identified from a cluster analysis of seismic tomography models (Lekic et al., 2012).

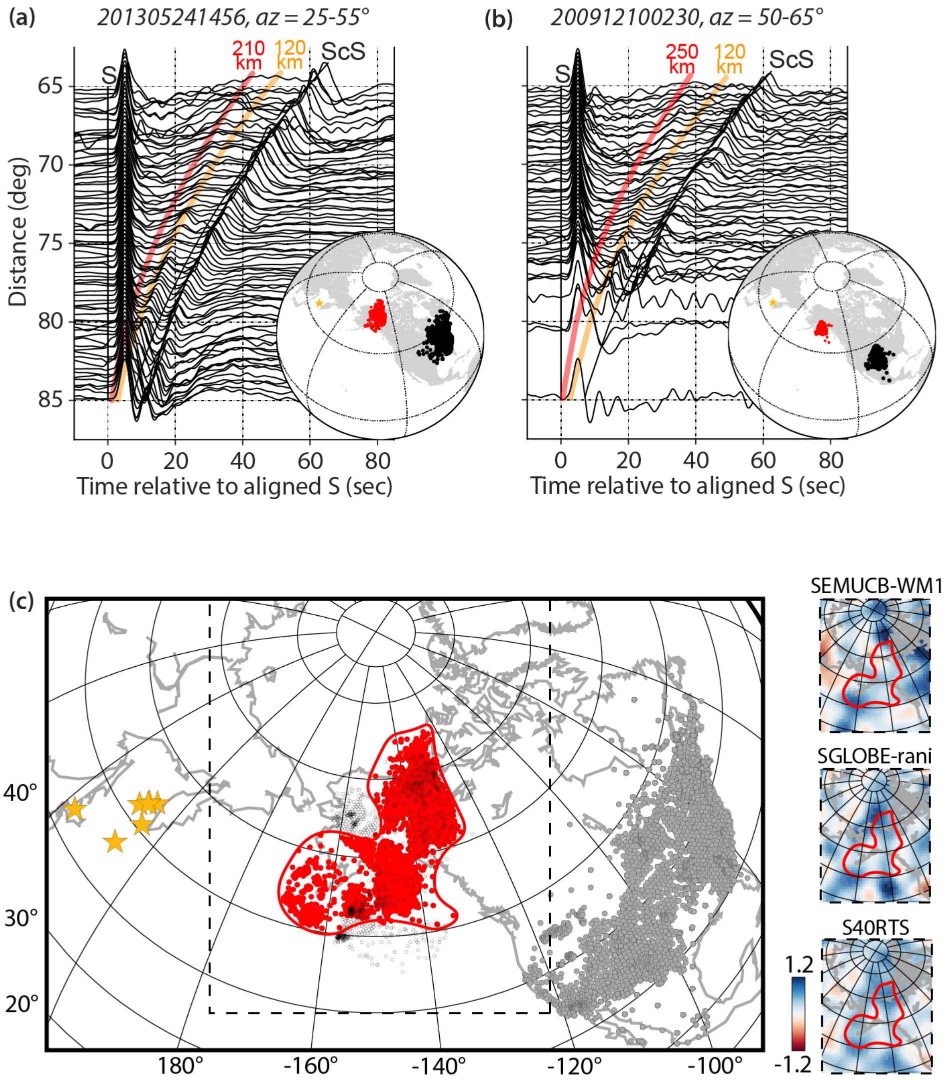

Figure 2. D″-discontinuity results. (a) Transverse displacement waveform stacks at 0.2° distance increments for an event on May 24, 2013, in the Sea of Okhotsk, recorded across the United States. Waveforms are aligned on the S arrival. Colored lines mark predicted arrival times for D″ reflections 210 km (red) and 120 km (yellow) above the CMB. Inset: Map showing the event (yellow star), stations (black circles), and D″ reflection points (red circles). (b) Same as (a), but for an event on December 12, 2009. The red line marks the SdS arrival time for a D″ boundary 250 km above the CMB. (c) Left: Map of all events (yellow stars) and stations (gray circles) used in this study. Red circles mark D″ locations (calculated along the great-circle path) where reflections are detected; black open circles denote paths with no detected reflection (though absence of detection does not imply absence of the boundary; see text). Right: Tomographic depth slices at 2800 km through three seismic models (legend) (French & Romanowicz, 2014; Chang et al., 2015; Ritsema et al., 2011), all showing high seismic velocities in the study region. Red outline highlight regions where a D″ reflector is observed.

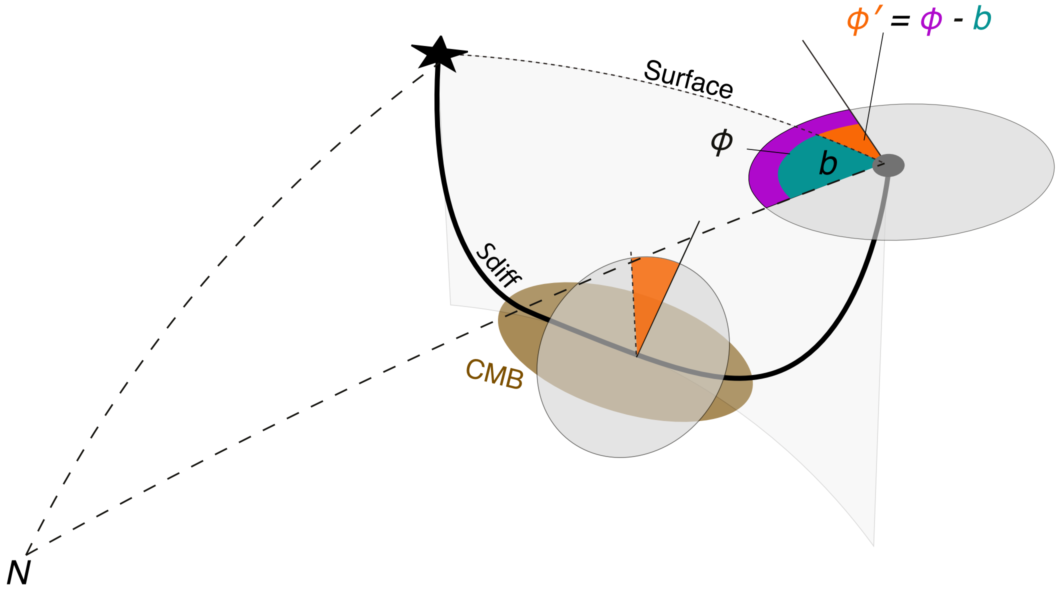

Figure 3. Definition of the polarization direction ϕ' for the S_{diff}phase. The S_{diff} raypath (black line) travels from the event (black star) along the core-mantle boundary (CMB; brown) to the station (gray circle). The fast polarization direction ϕ' is measured relative to the backazimuth (b), whereas ϕ is referenced to geographic North (N). Therefore, $\phi' = 0^\circ$ corresponds to a vertical fast polarization direction at the CMB, while $\phi' = \pm 90^\circ$ corresponds to a horizontal fast direction.

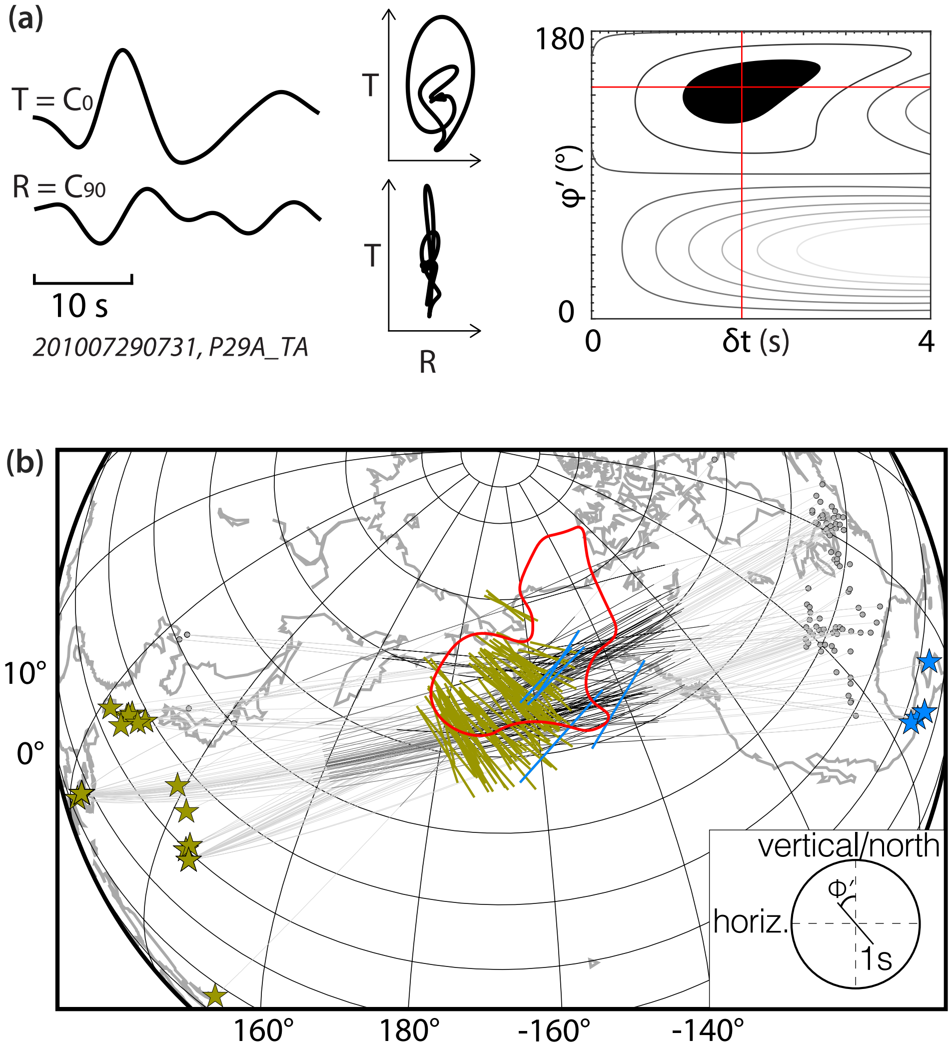

Figure 4. Summary of S_{diff} splitting results. (a) S_{diff} splitting example. Left: Transverse (C_0) and radial (C_{90}) waveforms. Middle: Particle motion before (top) and after (bottom) correcting for optimal splitting parameters. Right: Best-fitting splitting parameters, ϕ' and δt (red cross), and the corresponding 95% confidence region (black shaded region). (b) Map of all S_{diff} splitting measurements. Gray circles denote stations, and stars mark events. Splitting parameters are depicted as sticks, centered at the location where S_{diff} leaves the CMB. Colors denote the sampling azimuth of the study region (dark yellow or blue). Stick orientation represents ϕ' (Figure 3), and length corresponds to δt (legend). Note that while splitting measurements are centered at the mid-point of ray-theoretical S_{diff} sensitivity in D″, they are not plotted in the geographic reference frame; instead, the geographic North direction corresponds to $\phi' = 0°$ (legend). Light gray lines trace great-circle ray paths. Dark gray segments mark the diffraction distance of the S_{diff} wave along the CMB, while black lines show the receiver-side ray path through the D″ layer (assumed to be 250 km above the CMB). The red outline bounds the region where the D″ discontinuity is detected (Figure 1).

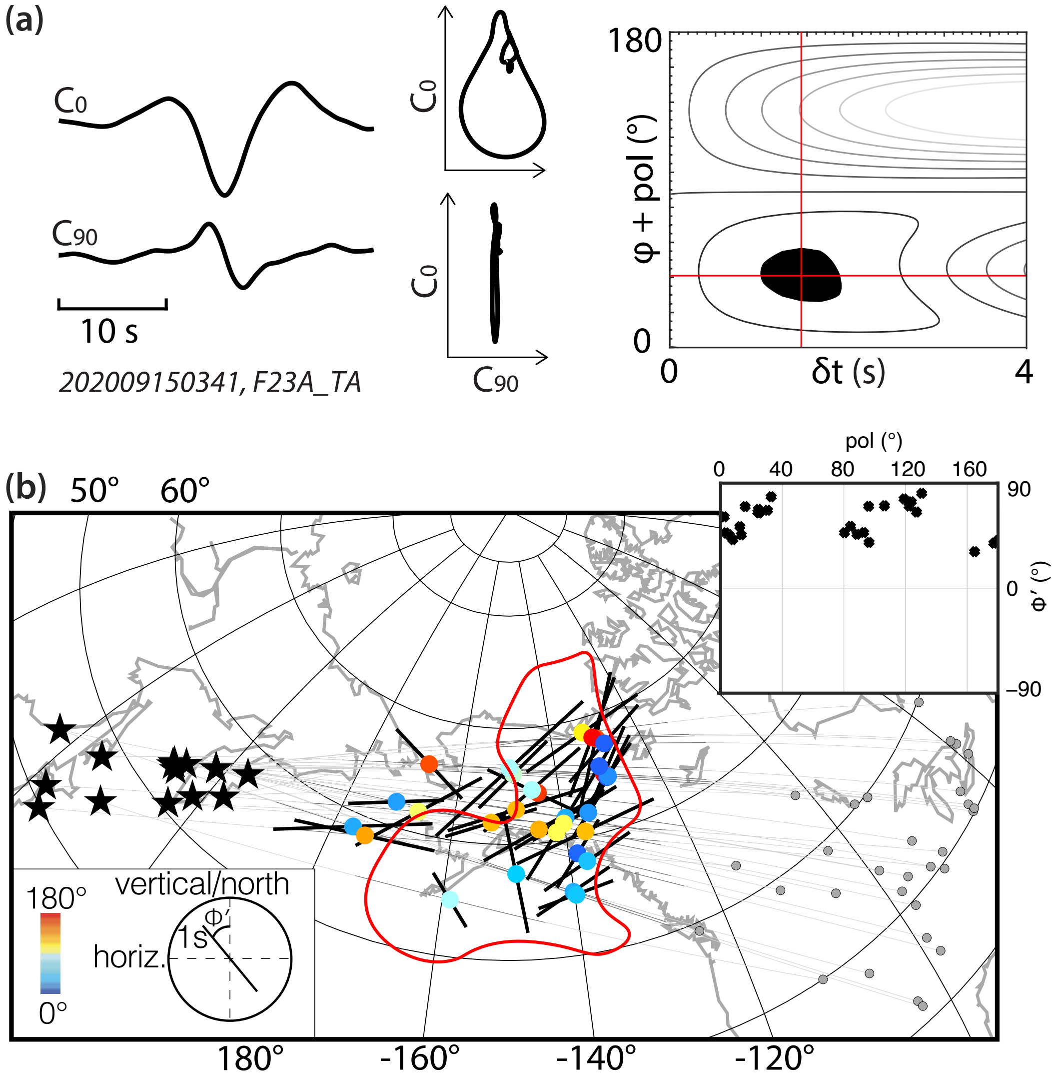

Figure 5. Summary of ScS splitting results. (a) ScS splitting example. Left: Transverse (C_0) and radial (C_{90}) waveforms (see text). Middle: Particle motion before (top) and after (bottom) correcting for optimal splitting parameters. Right: Best-fitting splitting parameters, ϕ' and δt (red cross), and the corresponding 95% confidence region (black shaded region). (b) All ScS splitting measurements. Gray circles denote stations, and black stars mark events. Splitting parameters are depicted as black sticks, centered at the ScS reflection point on the CMB. Stick orientation represents ϕ' (angle clockwise from vertical), and length corresponds to δt (legend). Light gray lines trace great-circle raypaths; dark gray segments mark the part of the raypath through the lowermost 250 km of the mantle. Colored circles indicate ScS polarization, determined from the long axis of the particle motion ellipse (legend) at the CMB reflection point. The dependence of ϕ' on the ScS polarization is shown in the inset at top left. The red outline bounds the region where the D$''$ discontinuity is detected (Figure 1).

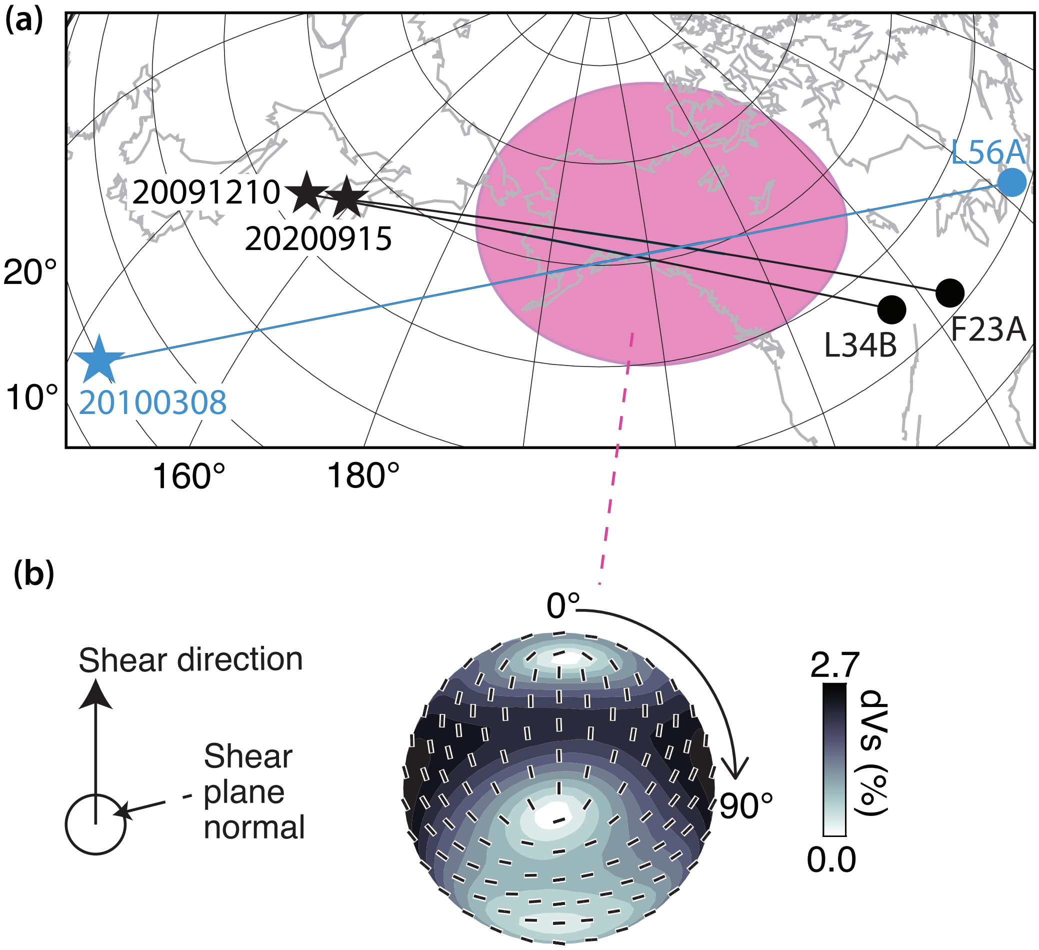

Figure 6. Setup for synthetic simulations. (a) Simulated events (stars) and corresponding receivers (circles), colored blue for S_{diff} and black for ScS. The extent of the anisotropic region implemented in the simulation is highlighted by pink shading. (b) Upper hemisphere representation of an example pPv elastic tensor used in the simulation. This tensor (dominant slip system of [100](010)) is from Creasy et al. (2020), who conducted visco-plastic self-consistent modeling based on the single-crystal elastic tensor proposed by Stackhouse et al. (2006). Black sticks show fast S-wave polarization directions, and background colors indicate the magnitude of V_S anisotropy (in %) for each direction (legend). The model assumes a horizontal shear plane, with the tensor rotated clockwise from North to explore different potential shear directions.

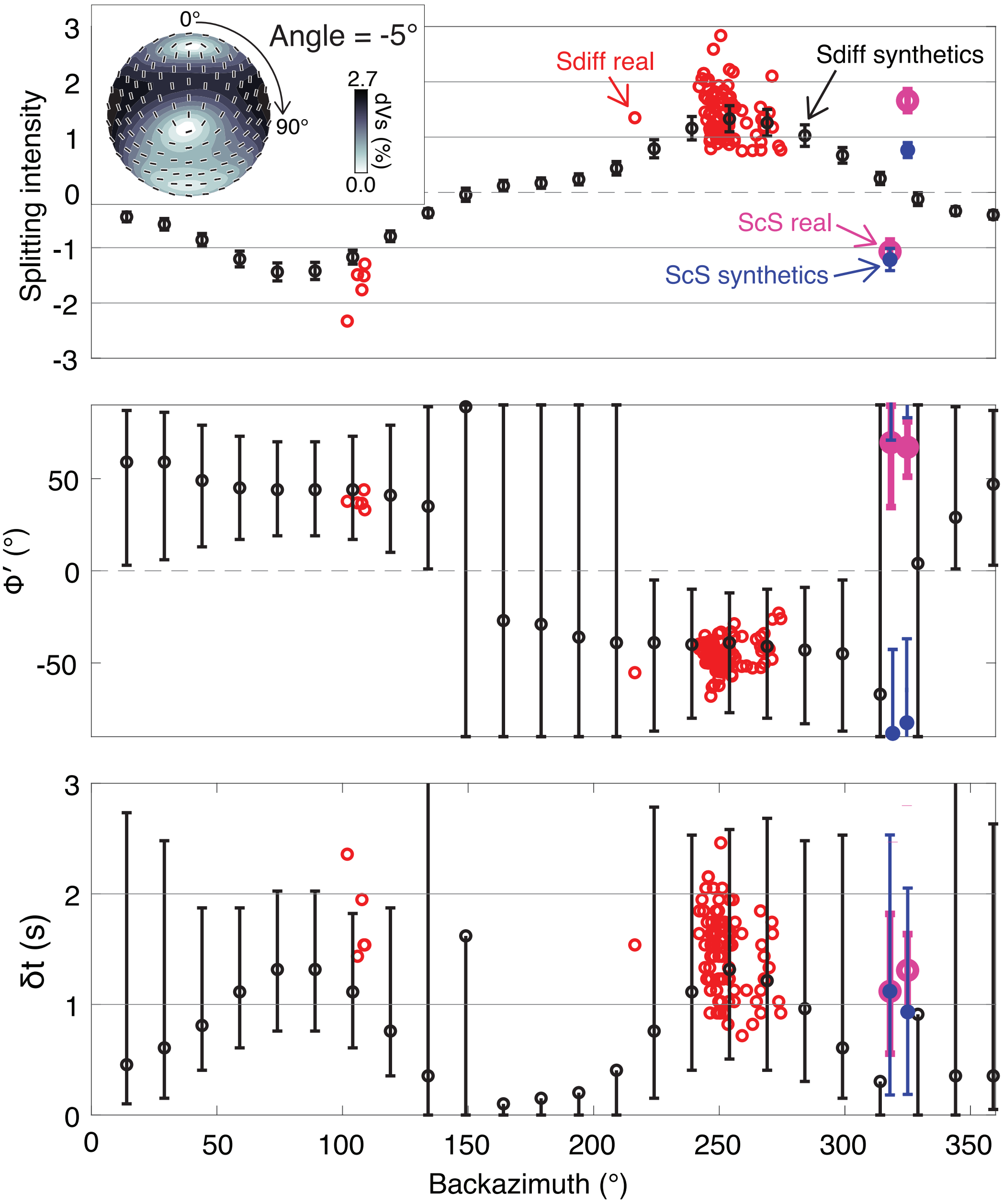

Figure 7. Splitting parameters of synthetic seismograms (for setup, see Figure 6) and comparison to real-data results. The model assumes a pPv layer at the base of the mantle, described by the elastic tensor shown in Figure 6b (inset). Black markers with errorbars show the 95% confidence intervals for the synthetic measurements, displayed as a function of backazimuth for a slightly rotated elastic tensor (shear direction −5° relative to North). Real data S_{diff} measurements are shown as red circles. Synthetic ScS measurements for both events are shown in blue and real-data measurements in pink, with errorbars indicating 95% confidence intervals. Results for other elastic tensors are shown in Supplementary Figures S4-S7.

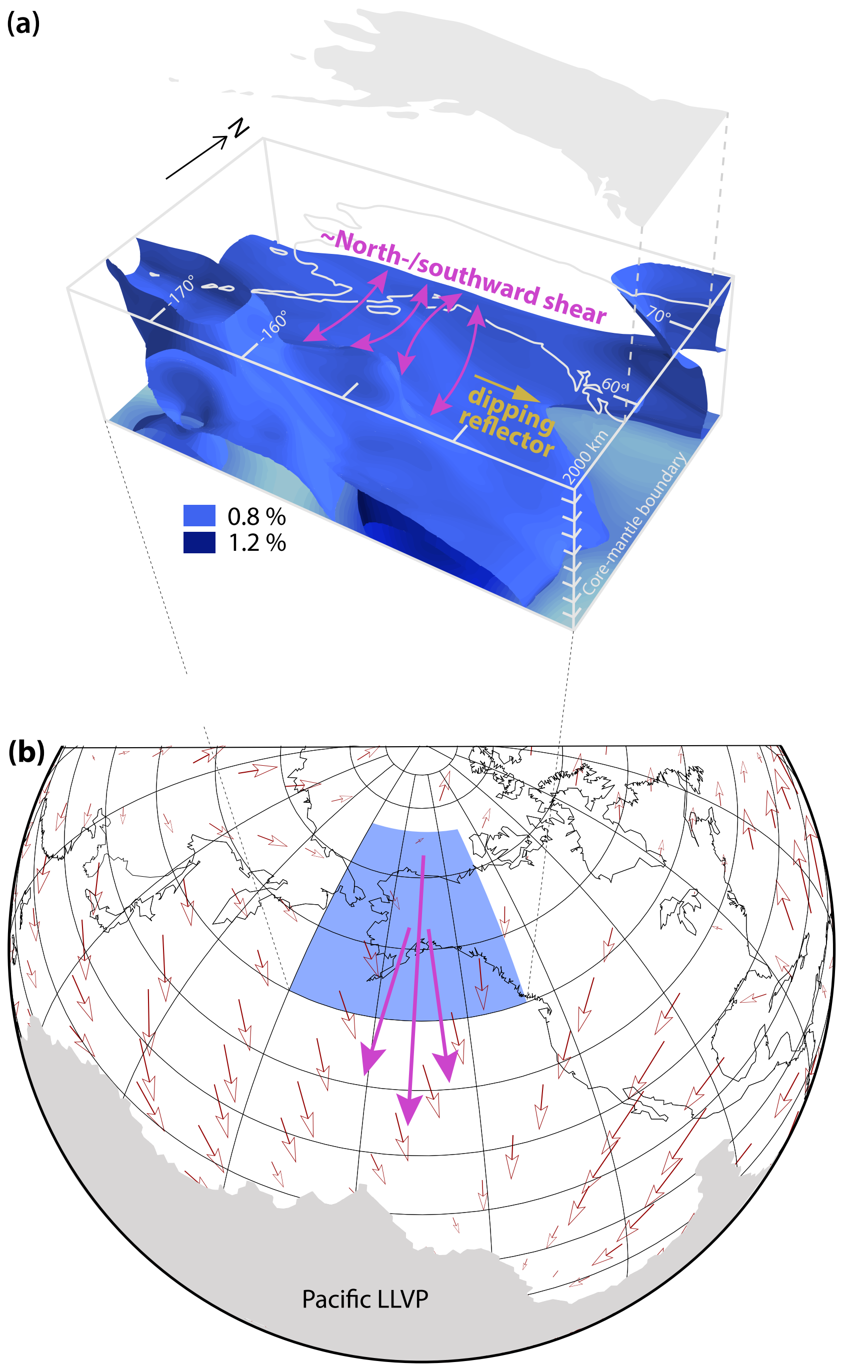

Figure 8. Summary of results and comparison to geodynamic flow predictions. (a) Colors (legend) show the 0.8% and 1.2% velocity perturbation isosurfaces from the GLAD-M25 tomographic model (Lei et al., 2020) beneath Alaska. Consistent with the reflection results presented here, the tomography model suggests fast velocities dipping to the east and a potentially larger velocity contrast in the east. The shear direction inferred from the seismic anisotropy analysis in this study is approximately southward (or, equivalently, northward). (b) Geodynamic modeling (Li et al., 2024) predicts large-scale flow (red arrows) directed toward the Pacific LLVP (gray). This is consistent with the shear direction inferred here beneath Alaska (blue region) and the findings of Wolf and Long (2022) beneath the northeastern Pacific Ocean (pink arrows).

References

Albuquerque Seismological Laboratory (ASL)/USGS. (1980). *US Geological Survey Networks.* International Federation of Digital Seismograph Networks. doi: 10.7914/SN/GS

Albuquerque Seismological Laboratory (ASL)/USGS. (1990). *United States National Seismic Network.* International Federation of Digital Seismograph Networks. doi: 10.7914/SN/US

Albuquerque Seismological Laboratory (ASL)/USGS. (1994). *New England Seismic Network.* International Federation of Digital Seismograph Networks. doi: 10.7914/SN/NE

Albuquerque Seismological Laboratory (ASL)/USGS. (2003). *Intermountain West Seismic Network.* International Federation of Digital Seismograph Networks. doi: 10.7914/SN/IW

Albuquerque Seismological Laboratory (ASL)/USGS. (2006). *Caribbean Network.* International Federation of Digital Seismograph Networks. doi: 10.7914/SN/CU

Albuquerque Seismological Laboratory/USGS. (2014). *Global Seismograph Network (GSN - IRIS/USGS).* International Federation of Digital Seismograph Networks. doi: 10.7914/SN/IU

Anderson, D. L. (1995). Lithosphere, asthenosphere, and perisphere. *Reviews of Geophysics*, *33*(1), 125-149. doi: 10.1029/94RG02785

Asplet, J., Wookey, J., & Kendall, M. (2020). A potential post-perovskite province in D″ beneath the Eastern Pacific: evidence from new analysis of discrepant SKS–SKKS shear-wave splitting. *Geophysical Journal International*, *221*, 2075–2090. doi: 10.1093/gji/ggaa114

Asplet, J., Wookey, J., & Kendall, M. (2023). Inversion of shear wave waveforms reveal deformation in the lowermost mantle. *Geophysical Journal International*, *232*, 97–114. doi: 10.1093/gji/ggac328

Beyreuther, M., Barsch, R., Krischer, L., Megies, T., Behr, Y., & Wassermann, J. (2010). ObsPy: A Python Toolbox for Seismology. *Seismological Research Letters*, *81*, 530–533. (doi: 10.1111/10.1785/gssrl.81.3.530 [Software])

California Institute of Technology and United States Geological Survey Pasadena. (1926). *Southern California Seismic Network.* International Federation of

Digital Seismograph Networks. doi: 10.7914/SN/CI

Caltech. (2014). *Southern California Earthquake Center.* (doi: 10.7909/C3WD3xH1 [Dataset])

Cascades Volcano Observatory/USGS. (2001). *Cascade Chain Volcano Monitoring.* International Federation of Digital Seismograph Networks. doi: 10.7914/SN/CC

Chambers, K., & Woodhouse, J. H. (2006). Investigating the lowermost mantle using migrations of long-period s–scs data. *Geophysical Journal International*, *166*(2), 667-678. doi: 10.1111/j.1365-246X.2006.03002.x

Chang, S.-J., Ferreira, A. M. G., Ritsema, J., van Heijst, H. J., & Woodhouse, J. H. (2015). Joint inversion for global isotropic and radially anisotropic mantle structure including crustal thickness perturbations. *Journal of Geophysical Research: Solid Earth*, *120*, 4278–4300. doi: 10.1002/2014JB011824

Chevrot, S. (2000). Multichannel analysis of shear wave splitting. *Journal of Geophysical Research: Solid Earth*, *105*, 21579–21590. doi: 10.1029/2000JB900199

Cobden, L., Thomas, C., & Trampert, J. (2015). Seismic Detection of Post-perovskite Inside the Earth. *The Earth's Heterogeneous Mantle: A Geophysical, Geodynamical, and Geochemical Perspective*, 391-440. doi: 10.1007/978-3-319-15627-9_13

Creasy, N., Miyagi, L., & Long, M. D. (2020). A Library of Elastic Tensors for Lowermost Mantle Seismic Anisotropy Studies and Comparison With Seismic Observations. *Geochemistry, Geophysics, Geosystems*, *21*, e2019GC008883. doi: 10.1029/2019GC008883

Creasy, N., Pisconti, A., Long, M. D., Thomas, C., & Wookey, J. (2019). Constraining lowermost mantle anisotropy with body waves: a synthetic modelling study. *Geophysical Journal International*, *217*, 766–783. doi: 10.1093/gji/ggz049

Dziewonski, A. M., & Anderson, D. L. (1981). Preliminary reference Earth model. *Physics of the Earth and Planetary Interiors*, *25*, 297–356. doi: 10.1016/0031-9201(81)90046-7

Ekström, G., Nettles, M., & Dziewonski, A. (2012). The global CMT project 2004–2010: Centroid-moment tensors for 13,017 earthquakes. *Physics of the*

Earth and Planetary Interiors, *200-201*, 1–9. doi: https://doi.org/10.1016/j.pepi.2012.04.002

Fernando, B., Wolf, J., Leng, K., Nissen-Meyer, T., Eaton, W., Styczinski, M., . . . Long, M. (2024). AxiSEM3D - an introduction to using the code and its applications. *EarthArXiv*. doi: https://doi.org/10.31223/X5TH7P

Fischer, K. M., Hawman, R. B., & Wagner, L. S. (2010). *Southeastern Suture of the Appalachian Margin Experiment.* International Federation of Digital Seismograph Networks. doi: 10.7914/SN/Z9_2010

Flament, N. (2018). Present-day dynamic topography and lower-mantle structure from palaeogeographically constrained mantle flow models. *Geophysical Journal International*, *216*(3), 2158–2182. doi: 10.1093/gji/ggy526

Ford, H. A., Long, M. D., He, X., & Lynner, C. (2015). Lowermost mantle flow at the eastern edge of the African Large Low Shear Velocity Province. *Earth and Planetary Science Letters*, *420*, 12–22. doi: 10.1016/j.epsl.2015.03.029

Ford, H. A., Long, M. D., & Wirth, E. A. (2016). Midlithospheric discontinuities and complex anisotropic layering in the mantle lithosphere beneath the Wyoming and Superior Provinces. *Journal of Geophysical Research: Solid Earth*, *121*(9), 6675–6697. doi: 10.1002/2016JB012978

Forte, A. M., Simmons, N. A., & Grand, S. P. (2015). Constraints on seismic models from other disciplines—Implications for the global mantle convective flow. In *Treatise on geophysics* (pp. 853–907). doi: 10.1016/B978-044452748-6.00027-4

French, S. W., & Romanowicz, B. A. (2014). Whole-mantle radially anisotropic shear velocity structure from spectral-element waveform tomography. *Geophysical Journal International*, *199*(3), 1303–1327. doi: 10.1093/gji/ggu334

Garnero, E. J., & Lay, T. (1997). Lateral variations in lowermost mantle shear wave anisotropy beneath the north Pacific and Alaska. *Journal of Geophysical Research: Solid Earth*, *102*. doi: 10.1029/96JB03830

Gary Pavlis, & Hersh Gilbert. (2011). *Ozark Illinois Indiana Kentucky (OIINK) Flexible Array Experiment.* International Federation of Digital Seismograph Networks. doi: 10.7914/SN/XO_2011

Grand, S., & Ni, J. (2006). *Mapping the Rivera Subduction Zone.* International Federation of Digital Seismograph Networks. doi: 10.7914/SN/XF_2006

Hager, B. H., & O'Connell, R. J. (1979). Kinematic models of large-scale flow in the earth's mantle. *Journal of Geophysical Research: Solid Earth*, *84*(B3), 1031-1048. doi: 10.1029/JB084iB03p01031

Hu, M., & Gurnis, M. (2025). Edges of thermochemical structures in the lower mantle. *Physics of the Earth and Planetary Interiors*, *365*, 107381. doi: 10.1016/j.pepi.2025.107381

Hu, M., Gurnis, M., & Jackson, J. M. (2025). Influence of subduction history and mineral deformation on seismic anisotropy in the lower mantle. *Geophysical Journal International*, ggaf457. doi: 10.1093/gji/ggaf457

Instituto de Geofísica, Universidad Nacional Autónoma de México, México. (2024). *SSN: Servicio Sismológico Nacional.* (doi: 10.21766/SSNMX/SN/MX [Dataset])

IRIS Transportable Array. (2003). *USArray Transportable Array.* International Federation of Digital Seismograph Networks. doi: 10.7914/SN/TA

Klemperer, S., & Miller, K. (2010). *Flexarray 3D Passive Seismic Imaging of Core-Complex Extension in the Ruby Range Nevada.* International Federation of Digital Seismograph Networks. doi: 10.7914/SN/YX_2010

Komatitsch, D., Vinnik, L. P., & Chevrot, S. (2010). SHdiff-SVdiff splitting in an isotropic Earth. *Journal of Geophysical Research: Solid Earth*, *115*(B7). doi: 10.1029/2009JB006795

Lamont Doherty Earth Observatory (LDEO), Columbia University. (1970). *Lamont-Doherty Cooperative Seismographic Network.* International Federation of Digital Seismograph Networks. doi: 10.7914/SN/LD

Lay, T., & Helmberger, D. V. (1983). The shear-wave velocity gradient at the base of the mantle. *Journal of Geophysical Research: Solid Earth*, *88*(B10), 8160–8170. doi: 10.1029/JB088iB10p08160

Lay, T., & Young, C. J. (1991). Analysis of seismic SV waves in the core's penumbra. *Geophysical Research Letters*, *18*(8), 1373–1376. Retrieved from `https://doi.org/10.1029/91GL01691`

Lay, T., & Young, C. J. (1996). Imaging scattering structures in the lower mantle by migration of long-period S waves. *Journal of Geophysical Research: Solid Earth*, *101*(B9), 20023-20040. doi: 10.1029/96JB01887

Lei, W., Ruan, Y., Bozdağ, E., Peter, D., Lefebvre, M., Komatitsch, D., . . . Pugmire, D. (2020). Global adjoint tomography—model GLAD-M25. *Geophysical*

Journal International, *223*, 1–21. doi: 10.1093/gji/ggaa253

Lekic, V., Cottaar, S., Dziewonski, A., & Romanowicz, B. (2012). Cluster analysis of global lower mantle tomography: A new class of structure and implications for chemical heterogeneity. *Earth and Planetary Science Letters*, *357-358*, 68–77. doi: 10.1016/j.epsl.2012.09.014

Leng, K., Korenaga, J., & Nissen-Meyer, T. (2020). 3-D scattering of elastic waves by small-scale heterogeneities in the Earth's mantle. *Geophysical Journal International*, *223*(1), 502–525. Retrieved from `https://doi.org/10.1093/gji/ggaa331`

Leng, K., Nissen-Meyer, T., & van Driel, M. (2016). Efficient global wave propagation adapted to 3-D structural complexity: a pseudospectral/spectral-element approach. *Geophysical Journal International*, *207*(3), 1700-1721. doi: 10.1093/gji/ggw363

Leng, K., Nissen-Meyer, T., van Driel, M., Hosseini, K., & Al-Attar, D. (2019). AxiSEM3D: broad-band seismic wavefields in 3-D global earth models with undulating discontinuities. *Geophysical Journal International*, *217*(3), 2125-2146. doi: 10.1093/gji/ggz092

Li, M., Wolf, J., Garnero, E., & Long, M. (2024). Flow and deformation in Earth's deepest mantle from geodynamic modeling and implications for seismic anisotropy. *ESS Open Archive*. doi: 10.22541/essoar.171052495.57595075/v1

Link, F., Reiss, M. C., & Rümpker, G. (2022). An automatized XKS-splitting procedure for large data sets: Extension package for SplitRacer and application to the USArray. *Computers & Geosciences*, *158*, 104961. doi: 10.1016/j.cageo.2021.104961

Long, M. (2009). Complex anisotropy in D$''$ beneath the eastern Pacific from SKS–SKKS splitting discrepancies. *Earth and Planetary Science Letters*, *283*, 181-189. doi: 10.1016/j.epsl.2009.04.019

Long, M. (2009). Complex anisotropy in D$''$ beneath the eastern Pacific from SKS–SKKS splitting discrepancies. *Earth and Planetary Science Letters*, *283*, 181–189. doi: 10.1016/j.epsl.2009.04.019

Long, M. D. (2013). Constraints on subduction geodynamics from seismic anisotropy. *Reviews of Geophysics*, *51*(1), 76–112. doi: 10.1002/rog.20008

Matzel, E., Sen, M. K., & Grand, S. P. (1996). Evidence for anisotropy in the deep mantle beneath Alaska. *Geophysical Research Letters*, *23*(18), 2417–2420. doi: 10.1029/96GL02186

McNamara, A., van Keken, P., & Karato, S.-i. (2002). Development of anisotropic structure in the Earth's lower mantle by solid-state convection. *Nature*, *416*, 310–314. doi: 10.1038/416310a

McNamara, A. K., van Keken, P. E., & Karato, S.-i. (2003). Development of finite strain in the convecting lower mantle and its implications for seismic anisotropy. *Journal of Geophysical Research: Solid Earth*, *108*(B5). doi: 10.1029/2002JB001970

Meade, C., Silver, P. G., & Kaneshima, S. (2005). Laboratory and seismological observations of lower mantle isotropy. *Geophysical Research Letters*, *22*, 1293–1296. doi: 10.1029/95GL01091

Murakami, M., Hirose, K., Kawamura, K., Sata, N., & Ohishi, Y. (2004). Post-Perovskite Phase Transition in MgSiO3. *Science*, *304*, 855–858. doi: 10.1126/science.1095932

Natural Resources Canada (NRCAN Canada). (1975). *Canadian national seismograph network.* International Federation of Digital Seismograph Networks. doi: 10.7914/SN/CN

Niu, F., & Perez, A. M. (2004). Seismic anisotropy in the lower mantle: A comparison of waveform splitting of SKS and SKKS. *Geophysical Research Letters*, *31*. doi: 10.1029/2004GL021196

Northern California Earthquake Data Center. (2014). *Berkeley Digital Seismic Network (BDSN).* Northern California Earthquake Data Center. doi: 10.7932/BDSN

Nowacki, A., & Wookey, J. (2016). The limits of ray theory when measuring shear wave splitting in the lowermost mantle with ScS waves. *Geophysical Journal International*, *207*, 1573–1583. doi: 10.1093/gji/ggw358

Nowacki, A., Wookey, J., & Kendall, J.-M. (2010). Deformation of the lowermost mantle from seismic anisotropy. *Nature*, *467*, 1091–1094. doi: 10.1038/nature09507

Nowacki, A., Wookey, J., & Kendall, J.-M. (2011). New advances in using seismic anisotropy, mineral physics and geodynamics to understand deformation in the lowermost mantle. *Journal of Geodynamics*, *52*, 205–228. doi:

10.1016/j.jog.2011.04.003

Parisi, L., Ferreira, A. M. G., & Ritsema, J. (2018). Apparent Splitting of S Waves Propagating Through an Isotropic Lowermost Mantle. *Journal of Geophysical Research: Solid Earth*, *123*, 3909–3922. doi: 10.1002/2017JB014394

Penn State University. (2004). *Pennsylvania State Seismic Network.* International Federation of Digital Seismograph Networks. doi: 10.7914/SN/PE

Pisconti, A., Creasy, N., Wookey, J., Long, M. D., & Thomas, C. (2023). Mineralogy, fabric and deformation domains in D″ across the southwestern border of the African LLSVP. *Geophysical Journal International*, *232*, 705–724. doi: 10.1093/gji/ggac359

Reiss, M., & Rümpker, G. (2017). SplitRacer: MATLAB Code and GUI for Semiautomated Analysis and Interpretation of Teleseismic Shear-Wave Splitting. *Seismological Research Letters*, *88*, 392 -– 409. doi: 10.1785/0220160191

RESIF. (1995). *RESIF-RLBP French Broad-band network, RESIF-RAP strong motion network and other seismic stations in metropolitan France.* RESIF - Réseau Sismologique et géodésique Français. doi: 10.15778/RESIF.FR

Ritsema, J., Deuss, A., van Heijst, H. J., & Woodhouse, J. H. (2011). S40RTS: a degree-40 shear-velocity model for the mantle from new Rayleigh wave dispersion, teleseismic traveltime and normal-mode splitting function measurements. *Geophysical Journal International*, *184*(3), 1223–1236. doi: 10.1111/j.1365-246X.2010.04884.x

Romanowicz, B., & Wenk, H.-R. a. (2017). Anisotropy in the deep Earth. *Physics of the Earth and Planetary Interiors*, *269*, 58–90. doi: 10.1016/j.pepi.2017.05.005

Roy, P., Steinberger, B., Faccenda, M., & Pons, M. (2025a). Lowermost mantle flow at thermochemical piles constrained by shear wave anisotropy: Insights from combined geodynamic and mantle fabric simulations at global scale. *Geochemistry, Geophysics, Geosystems*, *26*, e2025GC012510. doi: https://doi.org/10.1029/2025GC012510

Roy, P., Steinberger, B., Faccenda, M., & Pons, M. (2025b). Modeling anisotropic signature of slab-induced mantle plumes from thermochemical piles in the lowermost mantle. *Geophysical Research Letters*, *52*, e2024GL113299. doi: https://doi.org/10.1029/2024GL113299

Scripps Institution of Oceanography. (1986). *Global Seismograph Network - IRIS/IDA.* International Federation of Digital Seismograph Networks. doi: 10.7914/SN/II

Stackhouse, S., Brodholt, J. P., & Price, G. D. (2006). Elastic anisotropy of FeSiO3 end-members of the perovskite and post-perovskite phases. *Geophysical Research Letters*, *33*. Retrieved from `10.1029/2005GL023887` doi: 10.1029/2005GL023887

Suzuki, Y., Kawai, K., & Geller, R. J. (2021). Imaging paleoslabs and inferring the Clapeyron slope in D″ beneath the northern Pacific based on high-resolution inversion of seismic waveforms for 3-D transversely isotropic structure. *Physics of the Earth and Planetary Interiors*, 106751. doi: 10.1016/j.pepi.2021.106751

Tanimoto, T., & Anderson, D. L. (1984). Mapping convection in the mantle. *Geophysical Research Letters*, *11*(4), 287-290. doi: 10.1029/GL011i004p00287

UC Berkeley Seismological Laboratory. (2014). *Northern California Earthquake Data Center.* (doi: 10.7932/NCEDC [Dataset])

UC San Diego. (1982). *ANZA Regional Network.* International Federation of Digital Seismograph Networks. doi: 10.7914/SN/AZ

University of Oregon. (1990). *Pacific Northwest Seismic Network - University of Oregon.* International Federation of Digital Seismograph Networks. doi: 10.7914/SN/UO

University of Washington. (1963). *Pacific Northwest Seismic Network - University of Washington.* International Federation of Digital Seismograph Networks. doi: 10.7914/SN/UW

van der Meer, D. G., van Hinsbergen, D. J., & Spakman, W. (2018). Atlas of the underworld: Slab remnants in the mantle, their sinking history, and a new outlook on lower mantle viscosity. *Tectonophysics*, *723*, 309–448. doi: 10.1016/j.tecto.2017.10.004

Walker, A. M., Forte, A. M., Wookey, J., Nowacki, A., & Kendall, J.-M. (2011). Elastic anisotropy of D″ predicted from global models of mantle flow. *Geochemistry, Geophysics, Geosystems*, *12*. doi: 10.1029/2011GC003732

Wang, Y., & Wen, L. (2004). Mapping the geometry and geographic distribution of a very low velocity province at the base of the Earth's mantle. *Journal of Geophysical Research: Solid Earth*, *109*. doi: 10.1029/2003JB002674

Ward, J., Walker, A. M., Nowacki, A., Panton, J., & Davies, J. H. (2024). The sensitivity of lowermost mantle anisotropy to past mantle convection. *Physics of the Earth and Planetary Interiors*, *356*, 107264. doi: 10.1016/j.pepi.2024.107264

Wessel, P., & Smith, W. H. F. (1998). New, improved version of generic mapping tools released. *Eos, Transactions American Geophysical Union*, *79*, 579–579. (doi: 10.1029/98EO00426 [Software])

Wolf, J., Becker, T. W., Garnero, E., Liu, K. H., & West, J. D. (2025). Comprehensive global dataset of uniformly processed shear-wave splitting measurements. *Geophysical Journal International*, 863–875. doi: 10.1093/gji/ggaf076

Wolf, J., Frost, D. A., Brewster, A., Long, M. D., Garnero, E., & West, J. D. (2024). Widespread D″ Anisotropy Beneath North America and the Northeastern Pacific and Implications for Upper Mantle Anisotropy Measurements. *Journal of Geophysical Research: Solid Earth*, *129*(10), e2024JB029516. doi: doi.org/10.1029/2024JB029516

Wolf, J., Frost, D. A., Long, M. D., Garnero, E., Aderoju, A. O., Creasy, N., & Bozdağ, E. (2023). Observations of Mantle Seismic Anisotropy Using Array Techniques: Shear-Wave Splitting of Beamformed SmKS Phases. *Journal of Geophysical Research: Solid Earth*, *128*(1), e2022JB025556. doi: 10.1029/2022JB025556

Wolf, J., Li, M., & Long, M. D. (2024). Low-velocity heterogeneities redistributed by subducted material in the deepest mantle beneath north america. *Earth and Planetary Science Letters*, *642*, 118867. doi: 10.1016/j.epsl.2024.118867

Wolf, J., Li, M., Long, M. D., & Garnero, E. (2024). Advances in mapping lowermost mantle convective flow with seismic anisotropy observations. *Reviews of Geophysics*, *62*, e2023RG000833. doi: 10.1029/2023RG000833

Wolf, J., & Long, M. (2024). ScS shear-wave splitting in the lowermost mantle: Practical challenges and new global measurements. *Seismica*. doi: 10.22541/au.169774188.89948976/v2

Wolf, J., & Long, M. D. (2022). Slab-driven flow at the base of the mantle beneath the northeastern Pacific Ocean. *Earth and Planetary Science Letters*, *594*, 117758. doi: 10.1016/j.epsl.2022.117758

Wolf, J., & Long, M. D. (2023). Lowermost mantle structure beneath the central Pacific Ocean: Ultralow velocity zones and seismic anisotropy. *Geochemistry,* *Geophysics, Geosystems*, *24*, e2022GC010853. doi: 10.1029/2022GC010853

Wolf, J., Long, M. D., Creasy, N., & Garnero, E. (2023). On the measurement of Sdiff splitting caused by lowermost mantle anisotropy. *Geophysical Journal International*. doi: 10.1093/gji/ggac490

Wolf, J., Long, M. D., & Frost, D. A. (2024). Ultralow velocity zone and deep mantle flow beneath the Himalayas linked to subducted slab. *Nature Geoscience*, 1–7. doi: 10.1038/s41561-024-01386-5

Wolf, J., Long, M. D., Leng, K., & Nissen-Meyer, T. (2022). Sensitivity of SK(K)S and ScS phases to heterogeneous anisotropy in the lowermost mantle from global wavefield simulations. *Geophysical Journal International*, *228*, 366–386. doi: 10.1093/gji/ggab347

Wolf, J., Romanowicz, B., Garnero, E., Zhu, W., & West, J. (2025). Patterns of deformation in the deepest mantle linked to ancient subduction. *EarthArXiv*. doi: 10.31223/X5JQ6W

Wookey, J., Kendall, J.-M., & Rümpker, G. (2005). Lowermost mantle anisotropy beneath the north Pacific from differential S-ScS splitting. *Geophysical Journal International*, *161*, 829–838. doi: 10.1111/j.1365-246X.2005.02623.x

Wysession, M. E., Langenhorst, A., Fouch, M. J., Fischer, K. M., Al-Eqabi, G. I., Shore, P. J., & Clarke, T. J. (1999). Lateral Variations in Compressional/Shear Velocities at the Base of the Mantle. *Science*, *284*(5411), 120–125. doi: https://doi.org/10.1126/science.284.5411.120

Large-scale flow toward low-velocity anomalies reconciles seismic and geodynamic constraints in the deepest mantle beneath Alaska – SI

Jonathan Wolf[1,2,3]

[1]Department of Earth and Planetary Sciences, University of California, Santa Cruz, CA 95064, USA
[2]Department of Earth and Planetary Science, University of California, Berkeley, CA 94720, USA
[3]Miller Institute for Basic Research in Science, Berkeley, CA 94720, USA

Supplementary Figures

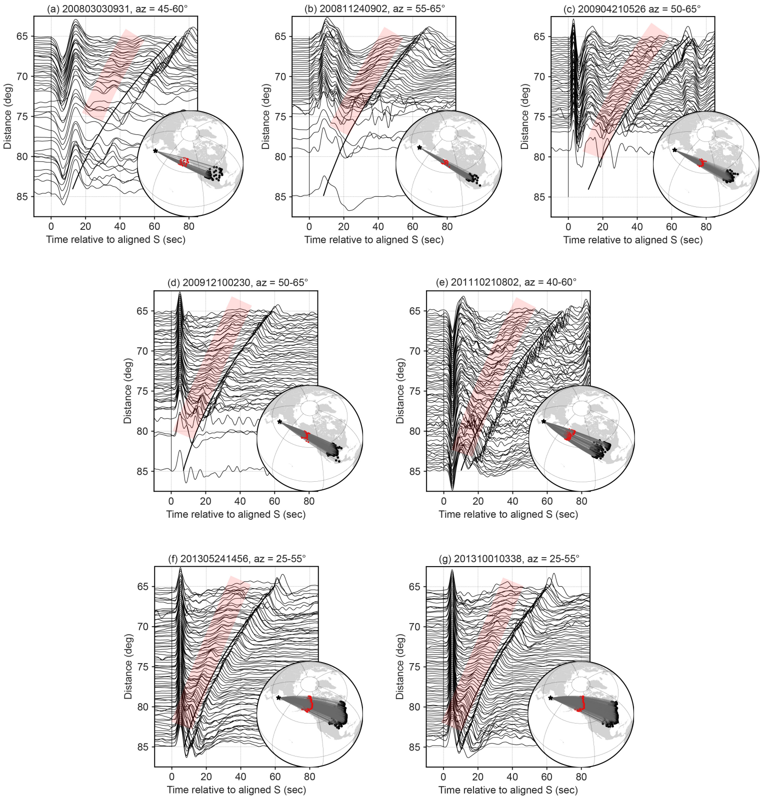

Figure S1. 0.2° distance-increment waveform stacks of transverse displacement seismograms (bandpass-filtered between 2 and 100 s) for all azimuths (a-g) for which a D$''$ reflection is detected. Waveforms are aligned on the S arrival. The identified D$''$ reflection is shown in red shading. Insets: Event (yellow star), stations (black circles), and D$''$ reflection points (red circles).

Corresponding author: Jonathan Wolf, `wolf@ucsc.edu`

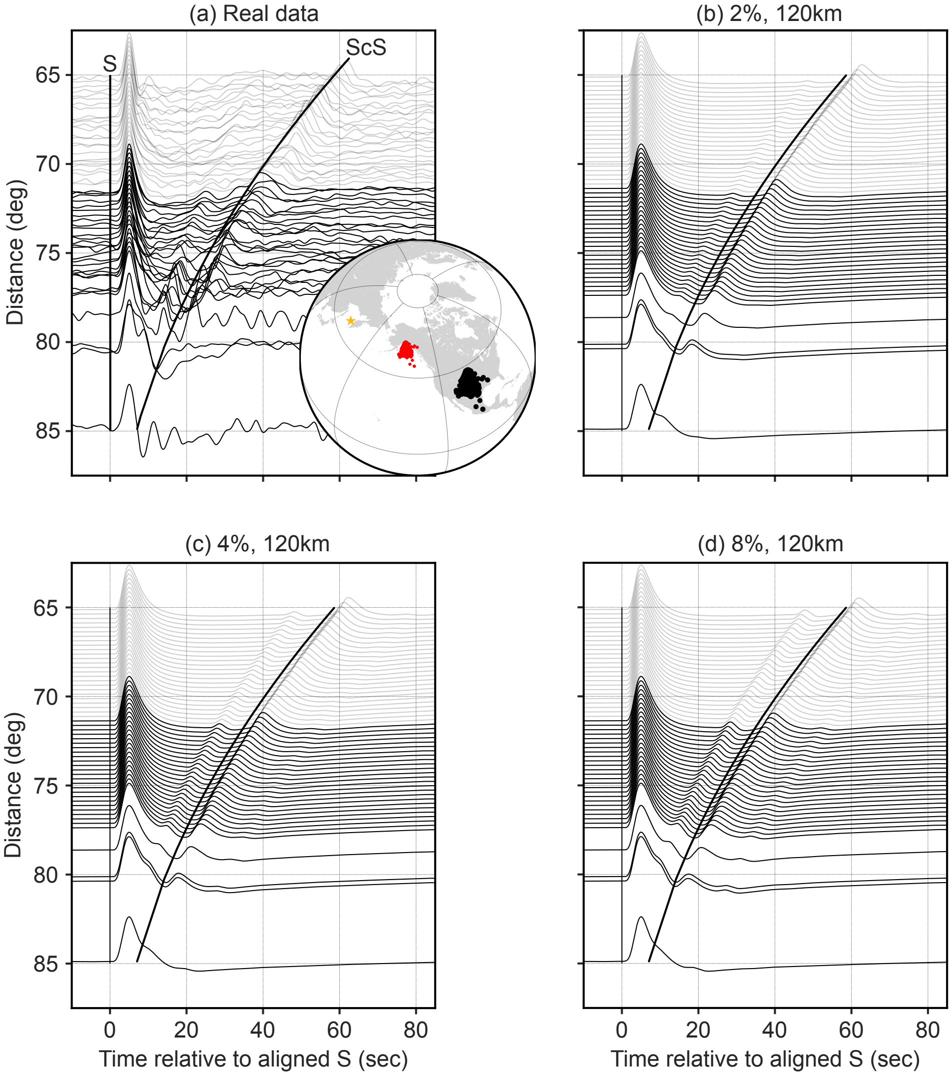

Figure S2. Wavefield simulations for different velocity contrasts across D″ for a layer thickness of 120 km, which fits well for the East of the study region. (a) Real-data results, displayed like in each panel of Figure S1. Only seismogram stacks for which the D″ reflection point is in the East of the study region are shown non-opaque. (b-d) Same as panel (a) for synthetic seismograms and different velocity contrasts across D″ (b: 2%, c: 4%, d: 8%).

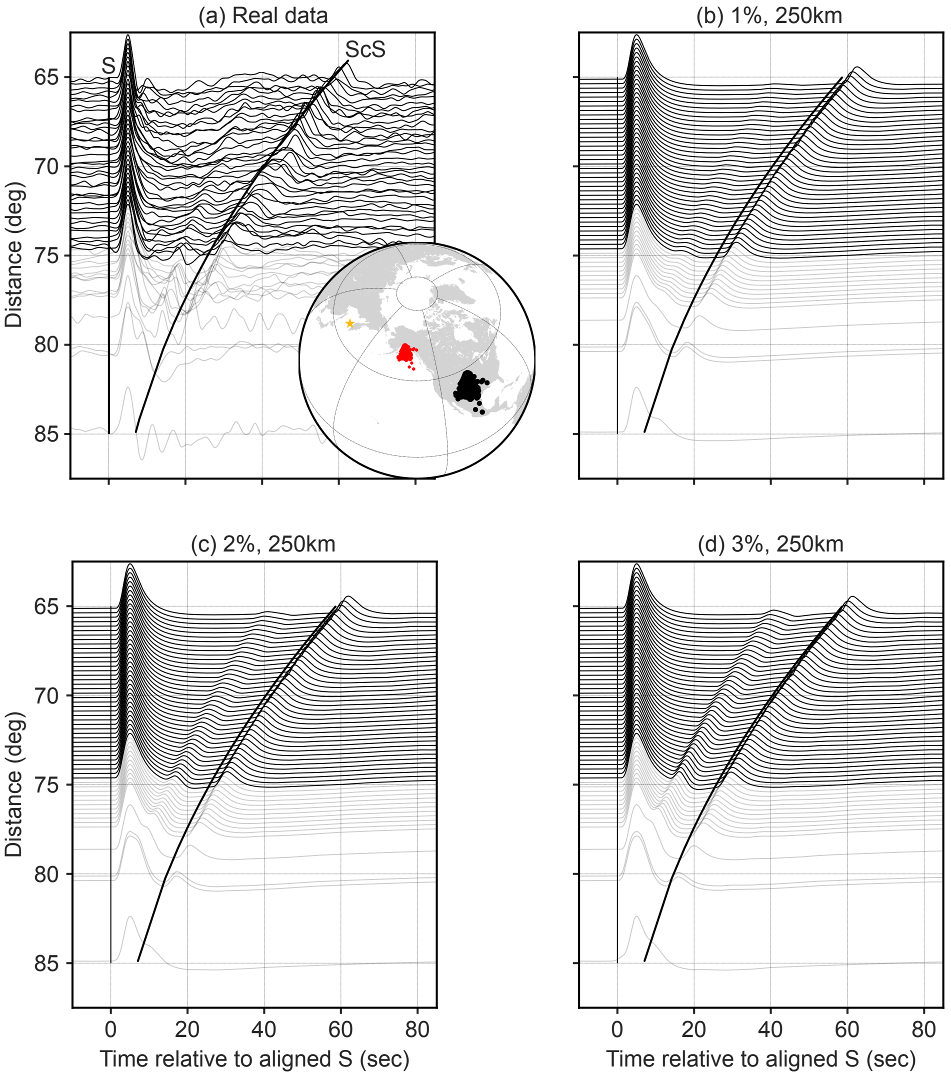

Figure S3. Wavefield simulations for different velocity contrasts across D$''$ for a layer thickness of 250 km, which fits well for the West of the study region. Plotting conventions are as in Figure S2.

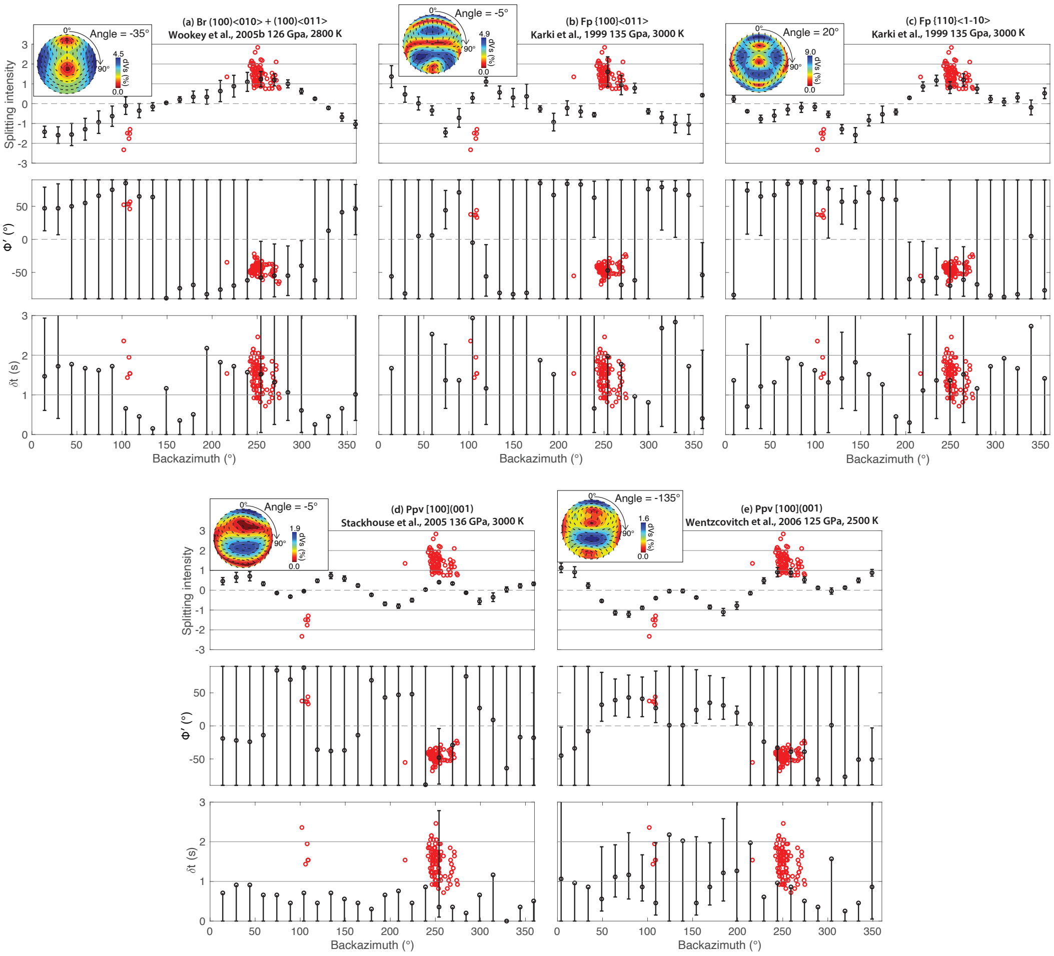

Figure S4. Splitting parameters of synthetic seismograms and comparison to real-data results for the elastic tensors that are unable to explain the observed S_{diff} splitting. (a) The header shows the mineral, dominant slip system, study that reported the single-crystal elastic tensor that the modeling results of Creasy et al. (2021) are based on, corresponding pressure and temperature conditions. Black markers with errorbars show the 95% confidence intervals for the synthetic measurements, displayed as a function of backazimuth for a rotated elastic tensor (shear direction of $-35°$ relative to North, displayed at top left). Real data S_{diff} measurements are shown as red circles. Inset: Upper hemisphere representation of elastic tensor used in the simulation. Black sticks illustrate the fast S-wave polarization directions, and the background colors represent the magnitude of V_s anisotropy (in %) for each direction. The model assumes a horizontal shear plane, with the tensor rotated clockwise from North to explore different potential shear directions. (b-e) Same plotting conventions as in panel (a) for different elastic tensors.

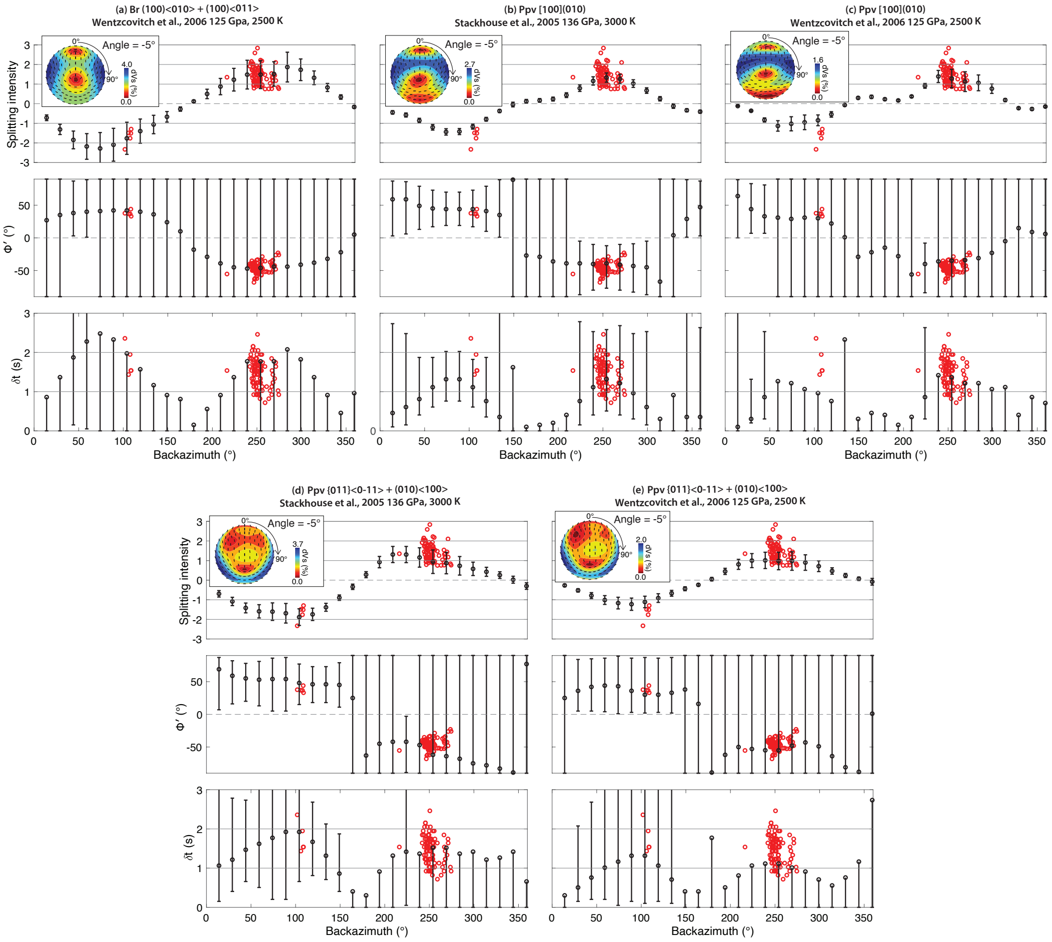

Figure S5. Splitting parameters of synthetic seismograms and comparison to real-data results for the elastic tensors that are able to explain the observed S_{diff} splitting. Plotting conventions are as in Figure S4.

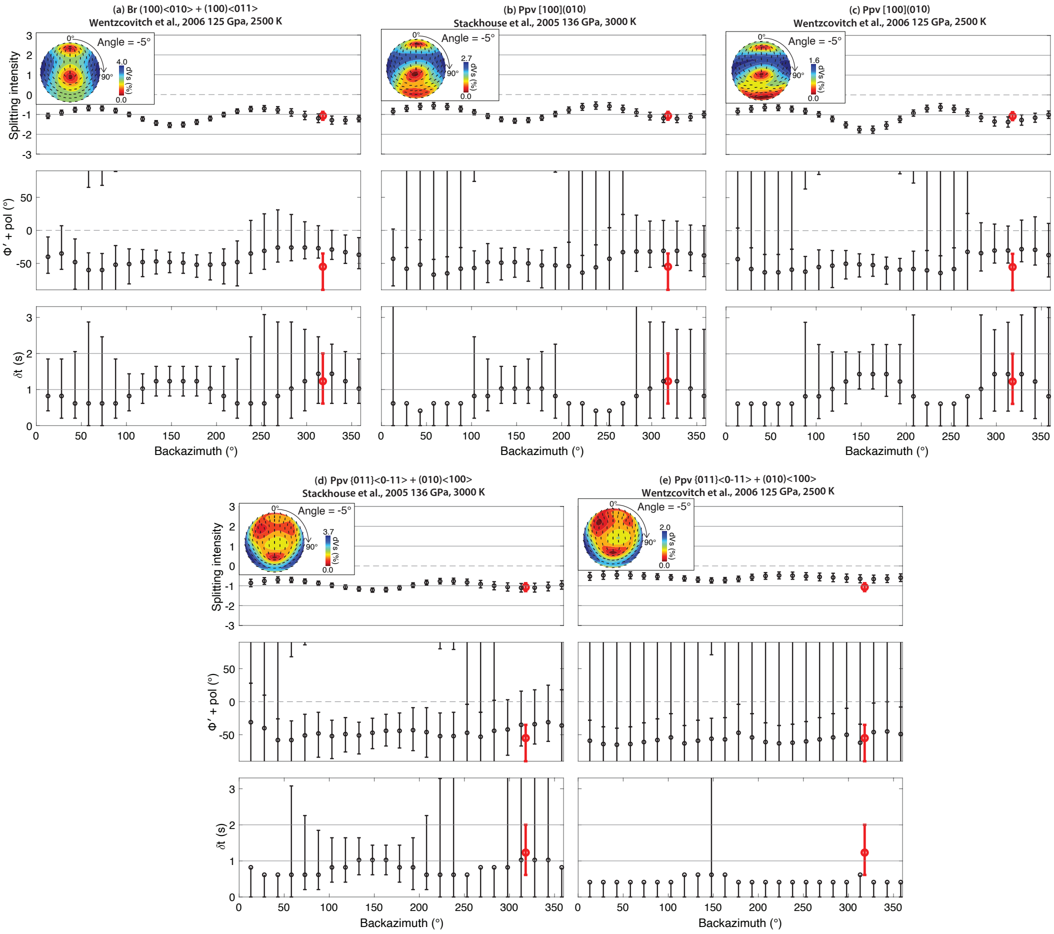

Figure S6. Splitting parameters of synthetic seismograms, measured from ScS, for those elastic tensors that are able to explain the $\mathrm{S_{diff}}$ splitting measurements. Synthetic simulations are conducted for the event that occurred on December 12, 2009, recorded at station F23A. ScS splitting parameters are plotted for the elastic tensor rotation that can explain $\mathrm{S_{diff}}$ measurements. (a) Same plotting convention as in Figure S4a, except the red measurement (errorbar: 95% confidence interval) represents the ScS measurements for the corresponding source-receiver configuration. (b-e) Same plotting conventions as in panel (a) for different elastic tensors.

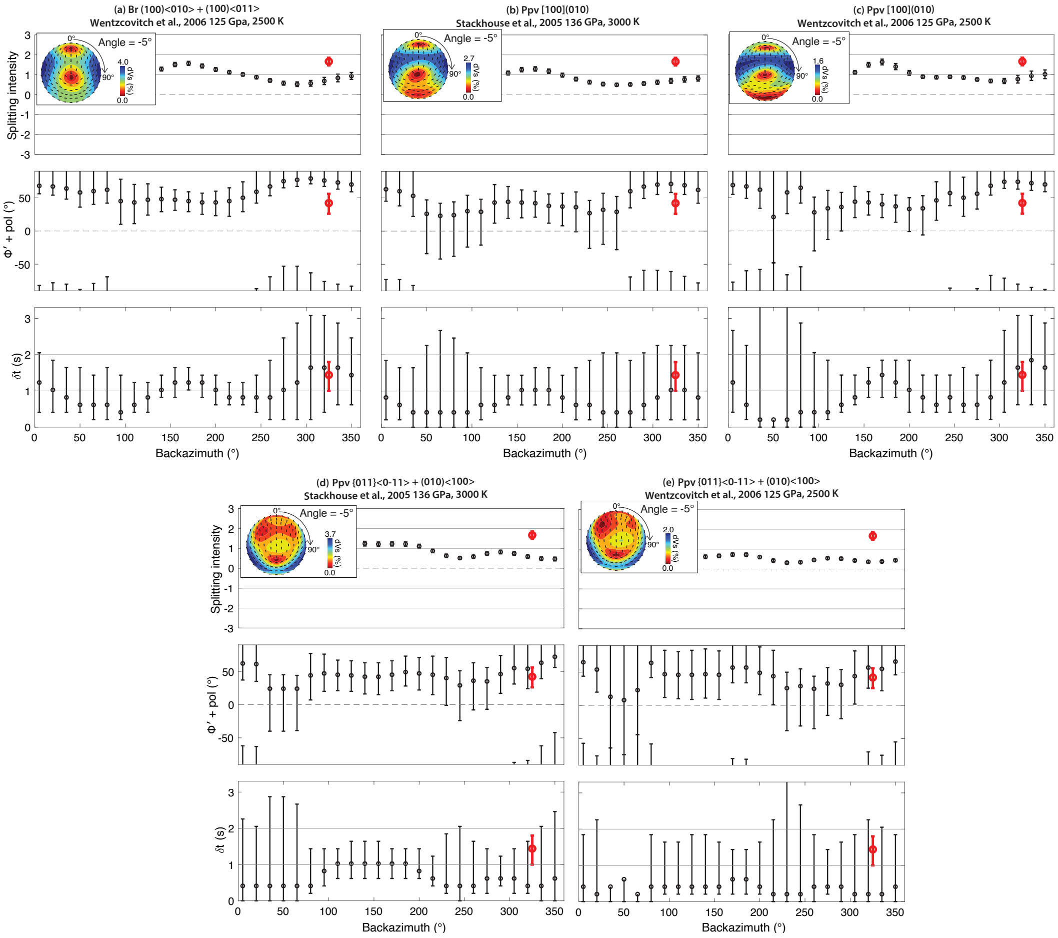

Figure S7. Splitting parameters of synthetic seismograms, measured from ScS, for those elastic tensors that are able to explain the S_{diff} splitting measurements. ScS splitting parameters are plotted for the elastic tensor rotation that can explain S_{diff} measurements. Synthetic simulations are conducted for the event that occurred on May 24, 2013, recorded at station L34B. The plotting conventions are identical to Figure S6.

References